Nanoscale

ROYAL SOCIETY OF CHEMISTRY

PAPER

View Article Online
View Journal | View Issue

Cite this: *Nanoscale*, 2025, **17**, 8084

Covalent functionalization of transition metal dichalcogenides with perylene for light harvesting devices†

Ruben Canton-Vitoria, *[a,b,c] Yuki Matsunaga,[b] Shaochun Zhang,[b] Mengsong Xue, [b] Minoru Osada [a,d,e] and Ryo Kitaura [b,f]

Received 20th December 2024,
Accepted 19th February 2025

DOI: 10.1039/d4nr05364h

rsc.li/nanoscale

This study investigates the optical and electronic properties of eight two-dimensional transition metal chalcogenides (TMDs)—MoS_2, WS_2, $MoSe_2$, WSe_2, $MoTe_2$, WTe_2, MoO_2, and WO_2—covalently functionalized with perylene, forming zero-dimensional/two-dimensional hybrid materials. Comprehensive characterization was conducted using techniques including XPS, Raman, EDX, TEM, and AFM. Optical properties were assessed using UV-Vis-NIR absorption and photoluminescence spectroscopy, while electronic properties were examined through cyclic voltammetry and field-effect transistor devices. Notably, the spectroscopic signatures of isolated perylene predominate in the hybrid materials, while WSe_2 and $MoSe_2$ displayed a novel band in the near-IR region, and $MoTe_2$ exhibited enhanced conductivity. Perylene significantly boosted absorption between 400–600 nm, leading to remarkable improvements in the photoresponse and responsivities showing values exceeding 2×10^5% and 2×10^4 mA W^{-1}, respectively. The presented hybrid materials rival the best examples of non-covalent functionalization, underscoring the potential of covalent functionalization as a powerful technique for further tailoring the optical and electronic properties of 2D materials.

1. Introduction

The properties of single-layer transition metal dichalcogenides (TMDs), including MoS_2, WS_2, $MoSe_2$, WSe_2, and $MoTe_2$, are well-documented and widely recognized.[1–3] TMDs exhibit either metallic or semiconducting properties, which can be precisely controlled during synthesis and further modified through temperature and chemical modulation.[3] The purest semiconducting phases are stable under ambient conditions for several months and can persist for years in the absence of oxygen.[4,5] WS_2 and WSe_2 have direct band gaps of 2.11 eV and 1.65 eV, with carrier mobilities of approximately 50 $cm^2\ V^{-1}\ s^{-1}$ and 180 $cm^2\ V^{-1}\ s^{-1}$, respectively.[6,7] Likewise, MoS_2 and $MoSe_2$ are generally n-type, with band gaps of 1.89 eV and 1.55 eV, and carrier mobilities exceeding 150 $cm^2\ V^{-1}\ s^{-1}$ and 50 $cm^2\ V^{-1}\ s^{-1}$, respectively.[8,9] For $MoTe_2$, the metallic phase is predominant; however, recent studies have successfully achieved the synthesis of the semiconducting phase through chemical vapor deposition (CVD). The semiconducting polytype of $MoTe_2$ exhibits a band gap ranging from 1.00 to 1.20 eV and a carrier mobility of 16.5 $cm^2\ V^{-1}\ s^{-1}$.[10] Conversely, WTe_2 is purely metallic, rendering its pristine phase less attractive for optical applications.[11] On the other hand, oxygen-based metal oxides, such as MoO_2 and WO_2, lack layered structures. Instead, ultrathin materials ranging from 1 to 100 nm in thickness have been synthesized using CVD, typically resulting in metallic properties.[12–15] Additionally, pristine TMDs devices exhibit promising performance as field-effect transistors (FETs), with on/off ratios exceeding 10^8[16] displaying n-type, p-type, or ambipolar behavior. Additionally, TMDs-based transistors are activated by light from the UV-Vis to near-IR regions, making them highly attractive for fabricating ultrasmall and ultraefficient flexible phototransistors.[17]

Exploring the properties of 2D-TMDs is a daunting task, given their complexity and extreme sensitivity. Due to their large surface area, 2D materials are highly susceptible to environmental interactions, leading to significant changes in properties that are influenced by factors such as the number of layers,[18] size,[19–21] strain,[22,23] defects,[24] temperature,[25] inter-

---

[a] Institute of Materials and Systems for Sustainability, Nagoya University, Nagoya 464-8601, Japan. E-mail: rcanton@imass.nagoya-u.ac.jp
[b] Department of Chemistry, Nagoya University, Nagoya, Aichi 464-8602, Japan
[c] Joining and Welding Research Institute, Osaka University, Osaka 567-0047, Japan
[d] Department of Materials Chemistry, Nagoya University, Nagoya 464-8601, Japan
[e] Research Institute for Quantum and Chemical Innovation, Institutes of Innovation for Future Society, Nagoya University, Nagoya 464-8601, Japan
[f] International Center for Materials Nanoarchitectonics, National Institute for Materials Science, 1-1 Namiki, Tsukuba 305-0044, Japan

† Electronic supplementary information (ESI) available. See DOI: https://doi.org/10.1039/d4nr05364h

layer angle,[26] substrate,[27] and polytype.[28] While minor variations can lead to substantial differences, complicating direct comparisons between studies, this inherent variability also offers distinct advantages. It enables the fine-tuning of TMDs properties, thereby broadening their potential applications. One of the most common strategies for tailoring the properties of TMDs involves doping, which can be either intrinsic,[29,30] altering the internal structure, or extrinsic,[2] modifying the surface environment. Focusing on the latter, modifications in the optoelectronic properties—such as absorption, photoemission, or photo-response—can also be achieved by anchoring organic molecules (0-dimensional structures) onto TMDs.[31] Examples include porphyrins,[32,33] phthalocyanines,[34–36] polyamide carbon dots,[37] fullerenes[38,39] pyrenes[40] or perylenes.[41] These modifications, achieved through simple interactions with other species, hold great promise in energy harvesting and nanotechnology. Unfortunately, the absence of π–π interactions in TMDs, compared to other nanomaterials like graphene, presents a challenge.[42] Aromatic molecules tend to self-assemble, causing substantial aggregation on the surface of TMDs and hindering their complete isolation.

Chemical functionalization ensures a strong bond, confining the organic molecules on the TMDs and enabling their complete isolation. This strategy has primarily been applied to MoS_2 and WS_2 rather than other TMDs.[43,44] Reactions involving sulfur derivatives, such as thiols,[45–47] dithiolanes,[48–50] sulfanes,[51] or dithioles,[52] are the most commonly used because they do not damage the material during the bonding process, unlike other method such as diazonium salt,[48] or decatungstate acylation.[53] Specifically, sulfur derivatives selectively target chalcogen vacancies without altering the crystallinity of the material. The level of functionalization achieved through sulfur derivative techniques tends to be low, but sufficient to isolate organic molecules on the TMDs surface, effectively forming a 0D–2D mixed material[54,55] and allowing for accurate examination using conventional methodologies. This approach has been used to study electron and energy transfer processes in MoS_2 and WS_2 with various organic molecules such as pyrene,[56–58] perylenes,[59] porphyrins,[55–61] or phthalocyanines,[62] as well as with 0D nanomaterials like fullerene derivatives[54] or polyamide carbon dots.[63] Moreover, covalently functionalized hybrid materials have demonstrated significant potential in areas such as catalysis,[50,61] and energy conversion.[56–62] Notably, MoS_2 and WS_2 exhibit distinctive and unique characteristics after functionalization with each chromophore, suggesting broader comparisons with other TMDs.[63]

Notably, the covalent functionalization of TMDs with organic chromophores for applications in optical nanodevices remains limited. Previous studies demonstrated that the photo-response of WS_2 doubles when functionalized with pyrene[56] under white light irradiation. This effect is further amplified when MoS_2 or WS_2 are functionalized with zinc porphyrin (ZnP)[55] or when MoS_2 or $MoSe_2$ are combined with PCBM,[54] improving the photo-response by more than tenfold and yielding final responsivities of 4.9×10^{-5}, 2.3×10^{-5}, 1.4, and 2.1×10^{-2} A W^{-1}, respectively. Moreover, the only electron-acceptor molecule tested so far is PCBM, a spherical molecule that hinders optimal contact with the 2D material. A planar molecule would enable better contact with 2D materials, as its entire π–π skeleton can be deposited on the TMDs surface, maximizing electronic interactions. In this context, perylene derivatives are electron-acceptor molecules with rich chemistry, making them promising candidates for further exploration.

To establish a standardized framework and advance the frontiers of covalent functionalization, we conducted an in-depth study of perylene modified with eight different 2D-TMDs materials. Specifically, we functionalized perylene derivatives with single layers of semiconducting MoS_2, $MoSe_2$, $MoTe_2$, WS_2, and WSe_2, as well as with metallic WTe_2, and ultrathin MoO_2 and WO_2. Our analysis focused on the electronic and optical properties, drawing attention to both the differences and similarities among the various functionalized TMDs. While perylene generally reduces the intrinsic emission of TMDs, we noted the emergence of new perylene-TMDs excitations, particularly in the selenide-based hybrid materials. Additionally, under light excitation at 450–550 nm, targeting perylene, the TMDs hybrids significantly alter their electronic states, largely enhancing the photo-response in MoS_2, $MoSe_2$, WSe_2, $MoTe_2$, and WO_2, whereas metallic WTe_2 and MoO_2 remained unaltered. Each hybrid material presents distinct advantages, targeting specific applications and proving attractive for various fields in nanotechnology.

2. Results and discussion

2.1 Synthesis

All TMDs (MoS_2, WS_2, $MoSe_2$, WSe_2, $MoTe_2$, WTe_2, MoO_2 and WO_2) were synthesized by CVD on SiO_2/Si substrates using our established CVD methodology (see Table S1†).[54] Next, 3,4,9,10-perylenetetracarboxylic dianhydride was coupled with cysteine *via* amidation, resulting in the formation of a perylene diamide bi-substituted.[64,65] Subsequently, the TMDs on the substrate were immersed in perylene and stirred slowly during 4 days at temperatures between 40–50 °C, resulting in the formation of Per-MoS_2, Per-WS_2, Per-$MoSe_2$, Per-WSe_2, Per-$MoTe_2$, Per-WTe_2, Per-MoO_2, and Per-WO_2 hybrid materials. After this period the non-covalent species were extensively cleaned with dimethylacetamide (DMAc). During the reaction, sulfur reacts with the chalcogen vacancies on the surface of the TMDs, resulting in the presence of perylene across the entire surface of the TMDs, as shown in Fig. 1. Due to the considerable length of perylene diimide between the two sulfur atoms, measuring 16.5 Å, it may cover a circular area of 854 $Å^2$. This increases the probability that both sulfur atoms will find basal vacancies to form covalent linkages, especially considering the high density of 2D chalcogen defects typically observed in TMDs, as reported in our previous studies.[54,55] Therefore, we will have a mixture in which a single or double sulfur of pery-

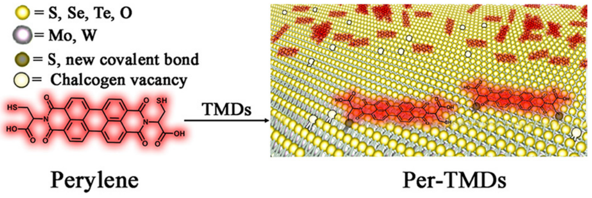

Fig. 1 Representative reaction route for obtaining Per-TMDs hybrids.

lene are covalently attached on TMDs. Additionally, the edges of TMDs, which contain more defects, will be functionalized but can also be considered negligible due to the large dimensions of our nanosheets.

2.2 Spectroscopic characterization

2.2.1 Raman. Raman spectra reveal the signatures of TMDs superimposed with those of perylene (see Fig. 2a). The A_{1g} mode, associated with out-of-plane vibrations of MoS_2,[55,57] WS_2,[54,55] $MoSe_2$,[66,67] WSe_2[68,69] and MoO_2,[70,71] are found at 408 cm^{-1}, 420 cm^{-1}, 240 cm^{-1}, 258 cm^{-1} and 583.2 cm^{-1}, respectively. On the other hand, the E^1_{2g} mode, related to the in-plane vibrations of MoS_2, WS_2, $MoSe_2$, WSe_2, and $MoTe_2$,[72] is observed at 383 cm^{-1}, 350 cm^{-1}, 287 cm^{-1}, 250 cm^{-1} and 232 cm^{-1}. Additionally, the 2LA(M) band, related to defects in the materials, is discernible for MoS_2, WS_2, and $MoSe_2$ at 460 cm^{-1}, 351.2 cm^{-1}, and 305 cm^{-1}, respectively. WTe_2,[73,74] MoO_2[70,71] and WO_2[14,15] are distinguished by a lack of deep spectroscopic characterization. However, peaks were observed at 135.8 cm^{-1} and 115.98 cm^{-1} for WTe_2, corresponding to the $^4A_1$ and $^3A_1$ modes. Peaks at 491 cm^{-1} and 740.8 cm^{-1} for MoO_2 are associated with the E_g and B_{2g} modes. Additionally, signatures at 169 cm^{-1}, 287 cm^{-1}, 349 cm^{-1}, 448 cm^{-1}, and 728 cm^{-1} were observed for WO_2. Next, perylene shown signatures at 1296 cm^{-1}, 1374 cm^{-1} and 1573 cm^{-1}.

After functionalization, some signatures of Per-MoS_2, such as the A_{1g} mode, shifted to 405 cm^{-1}, and the E^1_{2g} mode shifted to 381 cm^{-1}. Similar shifts were observed in Per-$MoSe_2$, Per-$MoTe_2$, Per-WTe_2, and Per-MoO_2, while the A_{1g} signature in Per-WS_2 decreased. Significantly, the 2LA(M)/A_{1g} ratio of MoS_2, WS_2, and $MoSe_2$ decreases by 30%, 300%, and 10%, respectively, after functionalization in Per-MoS_2, Per-WS_2, and Per-$MoSe_2$. We conducted the Raman measurements maintaining constant conditions to minimize variations related to environmental factors such as temperature, laser strength, or power effects.[18–28] Therefore, the primary cause of the Raman spec-

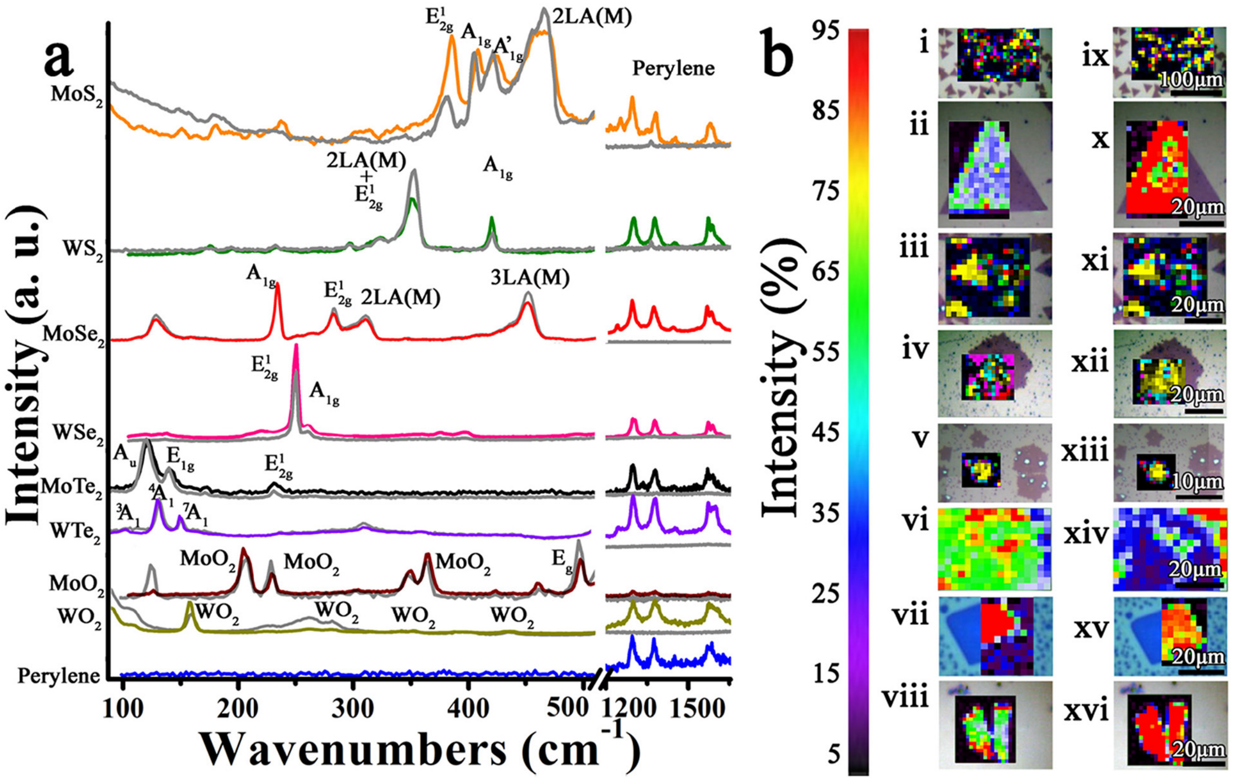

Fig. 2 (a) Raman spectra of Per-MoS_2 at 633 nm (orange), Per-WS_2 at 514 nm (olive), Per-$MoSe_2$ at 785 nm (red), Per-WSe_2 at 514 nm (pink), Per-$MoTe_2$ at 514 nm (black), Per-WTe_2 at 514 nm (purple), Per-MoO_2 at 514 nm (wine), Per-WO_2 at 514 nm (dark yellow), and perylene at 514 nm (blue). All materials have been normalized with pristine TMDs (gray) under the same conditions. (b) Raman spectroscopic mappings intensity showing the A_{1g} mode for Per-MoS_2 (i), Per-WS_2 (ii), Per-$MoSe_2$ (iii), the E^1_{2g} mode for Per-WSe_2 (iv), the A_u mode for $MoTe_2$ (v), the $^4A_1$ mode for Per-WTe_2(vi), the E_g mode for Per-MoO_2 (vii), and the peak at 169 cm^{-1} for Per-WO_2 (viii) and signature of perylene at 1296 for Per-MoS_2 (ix), Per-WS_2 (x), Per-$MoSe_2$ (xi), Per-WSe_2 (xii), $MoTe_2$ (xiii), MoO_2 (xv), and WO_2 (xvi), at the same excitation wavelength that (a).

tral changes is directly related to the addition of perylene. The shifts suggest electron doping between the two species, while the reduction of the LA(M) band indicates a decrease in the number of vacancies in the materials, likely due to the passivation of chalcogen vacancies by sulfur insertion, which supports the covalent functionalization. It should also be noted that perylene signatures were observed at 1296 cm^{-1}, 1374 cm^{-1}, and 1573 cm^{-1} across all Per-TMDs hybrid materials.

Fig. 2b shows the spectroscopic Raman mappings, highlighting the most intense modes of each TMDs and perylene. It is evident that the signatures of perylenes are exclusively on top of the nanosheets, suggesting that all non-covalently bonded species have been removed during the cleaning process, and only the strongly attached, covalently bound species remain.

2.2.2 IR and XPS.

IR spectroscopy reveals rich signatures of perylene diimide. However, this technique was not applicable for evaluating Per-TMDs hybrid materials. It should be noted that the single layers of TMDs are isolated over a large area on a robust SiO_2 substrate, which reduces detectivity. Consequently, the absence of the already weak S–H signature in perylene is likely due to it falling below the detection limit.

In contrast, X-ray photoelectron spectroscopy (XPS) offers valuable insights into the bonding nature within hybrid materials and is commonly used to chemically analyze the interactions between perylene and TMDs. Given the large number of materials studied, this manuscript focuses on a representative material, Per-MoS_2 (see Fig. 3), while the other hybrids and pristine materials are presented in Fig. S1.†

Firstly, the S 2p spectrum of pristine MoS_2 can be deconvoluted into five components: two peaks at 163.4 and 162.2 eV, which correspond to crystalline MoS_2, and two peaks at 163.1 and 161.9 eV, associated with sulfur vacancies (see Fig. 3a). All these bands exhibit similar areas, providing evidence that the basal plane of pristine MoS_2 contains significant defects. The fifth peak, observed at 168.0 eV, corresponds to oxidized sulfur species. After functionalization, the bands related to defects disappear, and the oxidized sulfur peak is significantly reduced(see Fig. 3a, inset). This result supports the occurrence of covalent functionalization between the cysteine groups of perylene and the defective regions of the material.[57] A similar description applies to WS_2.[56]

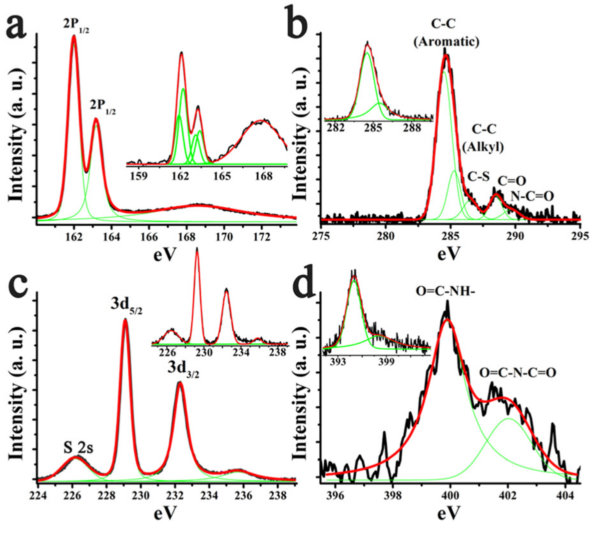

Fig. 3 XPS spectra for (a) S 2p, (b) C 1s, (c) Mo 3d, and (d) N 1s of Per-MoS_2, showing the acquired spectrum in black, deconvolution lines in green, and the sum of the spectra in red. The insets in Fig. 3 correspond to the XPS analysis of (a) S 2p, (b) C 1s, (c) Mo 3d, and (d) N 1s of pristine MoS_2.

The C–S–H bond from thiols, like free perylene, typically appears at ~164 eV, merging with the sulfur $2p_{1/2}$ peak in Per-MoS_2 or Per-WS_2, challenging its obtention.[56,57] In TMDs where the chalcogen is not sulfur, the thiol signature was only marginally observed, even though the presence of carbon and nitrogen confirms the presence of perylene, suggesting that has been employed for covering a chalcogen vacancy.[75] This phenomenon has been previously observed in other sulfur-free TMDs functionalized with sulfur derivatives.[54,76]

The C 1s signatures in all pristine TMDs appear broad and weak, indicating the presence of few amorphous carbon impurities. In contrast, the full width at half maximum (FWHM) of the carbon 1s peak at 284.73 eV is reduced in the hybrid materials at the same time that the intensity increases. Specifically, the FWHM of the carbon 1s peak ranges from 2.55 to 3.13 eV in pristine TMDs, whereas these values range from 1.33 to 1.88 eV in the hybrid materials. More notably, a new band at 288.55 eV and 286.55 confirms the presence of an amide bond (N–C═O) characteristic of perylene[77] and the C–S bound (see Fig. 3b). Similarly, the nitrogen 1s peak also exhibits a N–C═O band at 399.35 eV and an imine band at 402.00 eV (see Fig. 3d).[78,79] In conclusion, the covalent functionalization methodology has been unequivocally demonstrated.

For MoS_2,[80] $MoSe_2$,[79,81] $MoTe_2$,[82] and MoO_2,[83] strong signatures of molybdenum were recorded (see Fig. 3c and S1†). Specifically, the $3d_{5/2}$ peaks were observed at 229.25 eV, 228.61 eV, 228.23 eV, and 230.45 eV, while the $3d_{3/2}$ peaks appeared at 232.42 eV, 231.70 eV, 231.36 eV, and 233.00 eV, respectively. Additionally, an oxidized band related to MoO_3 species was recorded at 232.9 eV in $MoTe_2$.[54] This band is not associated with oxidized species within the structure of $MoTe_2$, but rather with the synthesis procedure, as $MoTe_2$ crystals grow hundreds of microns away from the bulk areas of MoO_3. Given that our incident laser has a diameter of 0.5 mm^2, we were unable to measure isolated crystals. In contrast, Raman spectroscopy confirms the absence of MoO_3 signatures once the surface of the layers is analyzed. This explanation also accounts for other oxide signatures, such as those recorded in WTe_2. The $4f_{7/2}$ peaks of tungsten (W) in WS_2,[5,84] WSe_2, WTe_2, and WO_2[85] were recorded at 32.83 eV, 32.79 eV, 31.58 eV, and 36.12 eV, respectively, while the $4f_{5/2}$ peaks appeared at 34.80 eV, 34.94 eV, 33.79 eV, and 38.19 eV.

The selenium $3d_{5/2}$ peaks in $MoSe_2$ and WSe_2 were observed at 54.30 eV and 54.60 eV, while the $3d_{3/2}$ peaks appeared at 54.98 eV and 55.35 eV, in the same order.[79,81] The tellurium

$3d_{5/2}$ peaks were observed at 574.15 eV for $MoTe_2$ and 572.54 eV for WTe_2,[54] while the $3d_{3/2}$ peaks were recorded at 584.61 eV for $MoTe_2$ and 583.06 eV for WTe_2. Oxygen 1s signatures in MoO_2[83] and WO_2[85] could be deconvoluted into two peaks, indicating interactions between oxygen and Mo or W. Specifically, the peak at 532.45 eV corresponds to the substrate, while the peaks at 530.78 eV and 531.01 eV are attributed to MoO_2 and WO_2, respectively.

After functionalization, the signatures of Mo, W, Se, Te, and O atoms show negligible spectral changes.[54] Thermogravimetric analysis (TGA) is widely employed to understand the level of functionalization in organic materials. However, this technique is not applicable to the current system. This is because the weight of the single-layer nanosheets (~1 nm) on the SiO_2 surface (1×10^6 nm thick) is negligible, making it impossible to obtain reliable data. On the other hand, the XPS intensities of each component enable the calculation of the level of perylenes onto TMDs. Per-$MoTe_2$ had the highest perylene loading, followed by Per-$MoSe_2$, Per-WS_2, Per-WSe_2, and Per-MoS_2, with ratios of 1 perylene per 8, 10, 20, 16, and 20 TMDs units, respectively. According to the unit cell dimensions of TMDs, the areas of MoS_2, WS_2, $MoSe_2$, WSe_2, and $MoTe_2$ are 8.66, 8.60, 9.43, 9.31, and 10.73 $Å^2$, respectively, while the area of perylene is approximately 40 $Å^2$. Therefore, a single perylene molecule can cover 4.6, 4.7, 4.2, 4.3 and 3.7 unit cells of MoS_2, WS_2, $MoSe_2$, WSe_2, and $MoTe_2$, respectively. 1 functional group of perylene per every 20 MoS_2, 20 WS_2, 10 $MoSe_2$, 16 WSe_2, and 8 $MoTe_2$ unit cells correspond to coverages of 23%, 23%, 42%, 26%, and 46%, respectively. This coverage is sufficient to detect perylene while ensuring that the molecules remain isolated. The results for other materials, such as MoO_2 and WO_2, are uncertain because they are not layered materials.

2.3 Morphological characterization

2.3.1 AFM. AFM reveals surface roughness on the nanosheets across all analyzed Per-TMDs, while the substrate remains unaffected, suggesting the presence of perylene exclusively on the basal plane of the nanosheets.[54,55,86] The variation in surface roughness is less than 3 nm, with these features uniformly distributed across the basal plane of the nanosheets. This suggests that perylenes form pseudo-monolayer films when covalently attached to Per-MoS_2, Per-WS_2, Per-$MoSe_2$, Per-WSe_2, Per-$MoTe_2$, or Per-WTe_2 (see Fig. 4a–f). The variation in the perylene nanofilm thickness by 1 to 2 nm can be attributed to the different ratio of chalcogen vacancies around the surface of the TMDs crystals. In materials with a higher number of chalcogen vacancies, the level of functionalization increases, causing perylene to adopt a vertical orientation rather than a horizontal one. This observation aligns with the dimensions of perylene ($0.3 \times 0.5 \times 1.6$ nm^3). Additionally, contact mode can sweep away any non-covalent functionalization species, ensuring that all the roughness observed is related to strong interactions between the organics and nanosheets.

Conversely, Per-MoO_2 and Per-WO_2 (Fig. 4g and h) lack a purely two-dimensional character, leading to the formation of ultrasmall 2D structures with thicknesses of approximately 15 nm and 50 nm, respectively.

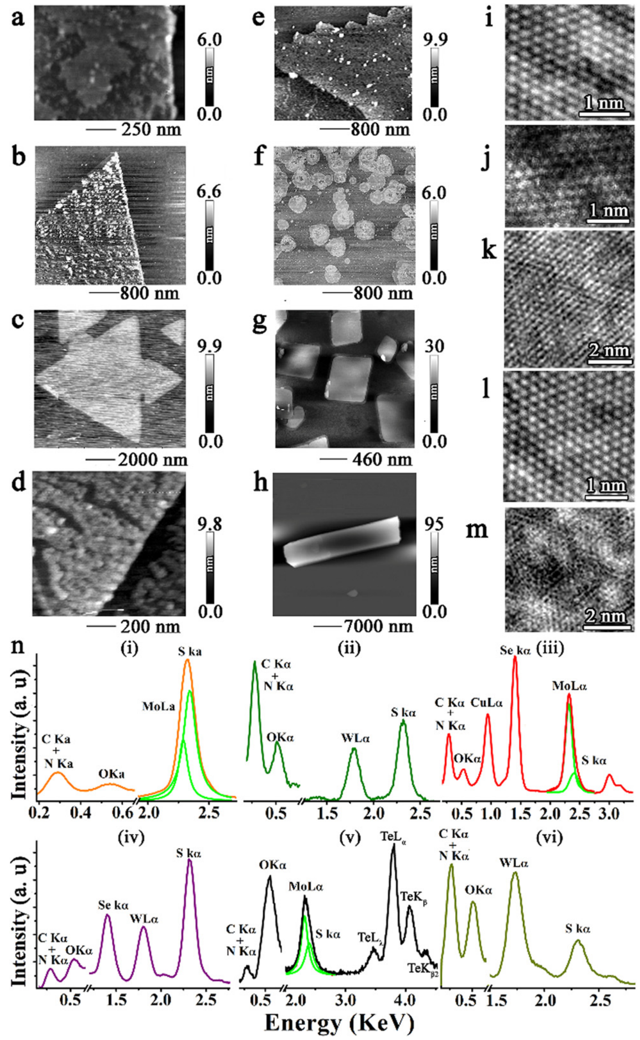

Fig. 4 AFM images at different magnifications for (a) Per-MoS_2, (b) Per-WS_2, (c) Per-$MoSe_2$, (d) Per-WSe_2, (e) Per-$MoTe_2$, (f) Per-WTe_2, (g) Per-MoO_2, and (h) Per-WO_2. High-magnification TEM images of (i) Per-MoS_2, (j) Per-WS_2, (k) Per-$MoSe_2$, (l) Per-WSe_2, and (m) Per-$MoTe_2$. (n) EDX mapping in the same regions for (i) Per-MoS_2, (ii) Per-WS_2, (iii) Per-$MoSe_2$, (iv) Per-WSe_2, (v) Per-$MoTe_2$ and (vi) Per-WO_2.

When Per-MoS_2, Per-WS_2, Per-$MoSe_2$, and Per-WSe_2 were annealed at 600 °C in the presence of the corresponding chalcogen, all the organic species associated with perylene were removed, recovering the original smooth surface characteristic of pristine TMDs (see Fig. S2a–d†). Additionally, pristine $MoTe_2$, MoO_2, and WO_2 can be observed in Fig. S2e–g.† In both cases, the thickness of the nanosheets is clearly reduced.

2.3.2 TEM. Transmission Electron Microscope (TEM) was used for atomic resolution imaging, clearly demonstrating that the hexagonal lattice characteristic of semiconducting TMDs is preserved after functionalization with perylene.[54,55] Atoms of molybdenum, tungsten, selenium, and tellurium were visualized at 1.5 million magnification, but lighter atoms such as sulfur, oxygen, carbon, and nitrogen show low contrast, making them invisible to our instrument. Consequently, the hybrid materials exhibited structures similar to those of the pristine materials (see Fig. 4i–m for Per-MoS_2, Per-WS_2, Per-$MoSe_2$, Per-WSe_2, and Per-$MoTe_2$, respectively). However, energy-dispersive X-ray spectroscopy (EDX) integrated into TEM confirms the presence of perylene in all TMDs. The studied transition metals (Mo or W) and chalcogens (O, S, Se, or Te) were shown with similar intensities. Additionally, carbon, nitrogen, oxygen, and sulfur were unambiguously detected on the basal plane of suspended TMDs, far from the amorphous carbon edges, confirming the incorporation of perylene into all Per-TMDs (see Fig. 4n).

2.4 Optical properties

2.4.1 Absorption. UV-Vis-Near-IR spectroscopy confirms the semiconducting nature of MoS_2, WS_2, $MoSe_2$, WSe_2, and $MoTe_2$, as these materials exhibit pronounced absorption bands between 400 nm and 1205 nm (Fig. 5a). Semiconducting TMDs typically exhibit two excitonic transition bands at lower energies, associated with spin–orbit splitting, and additional bands at higher energies corresponding to electronic transitions between the highest energy states in the valence band and the lowest energy states in the conduction band.[87] For MoS_2,[19] the bands were recorded at 397, 445, 611, and 673 nm while for WS_2[20] are found at 422, 459, 529, and 640 nm. Next, $MoSe_2$[54] exhibited bands at 453, 710, and 816 nm, and WSe_2[54] at 430, 631 and 690 nm. In addition, $MoTe_2$ also shows the semiconducting polytype with bands at 684, 935, and 1205 nm.[54] The absence of any bands in MoO_2, WO_2, or WTe_2 can be attributed to their metallic character.[54]

The bands of perylene were observed at 484, 514, and 559 nm in liquid media, corresponding to the electronic S_{0-1} transitions at 0–0, 0–1, and 0–2 vibrations, respectively.[59,88,89] In contrast, in solid states, the bands appeared very broad, merging and becoming almost indistinguishable (see Fig. 5a).

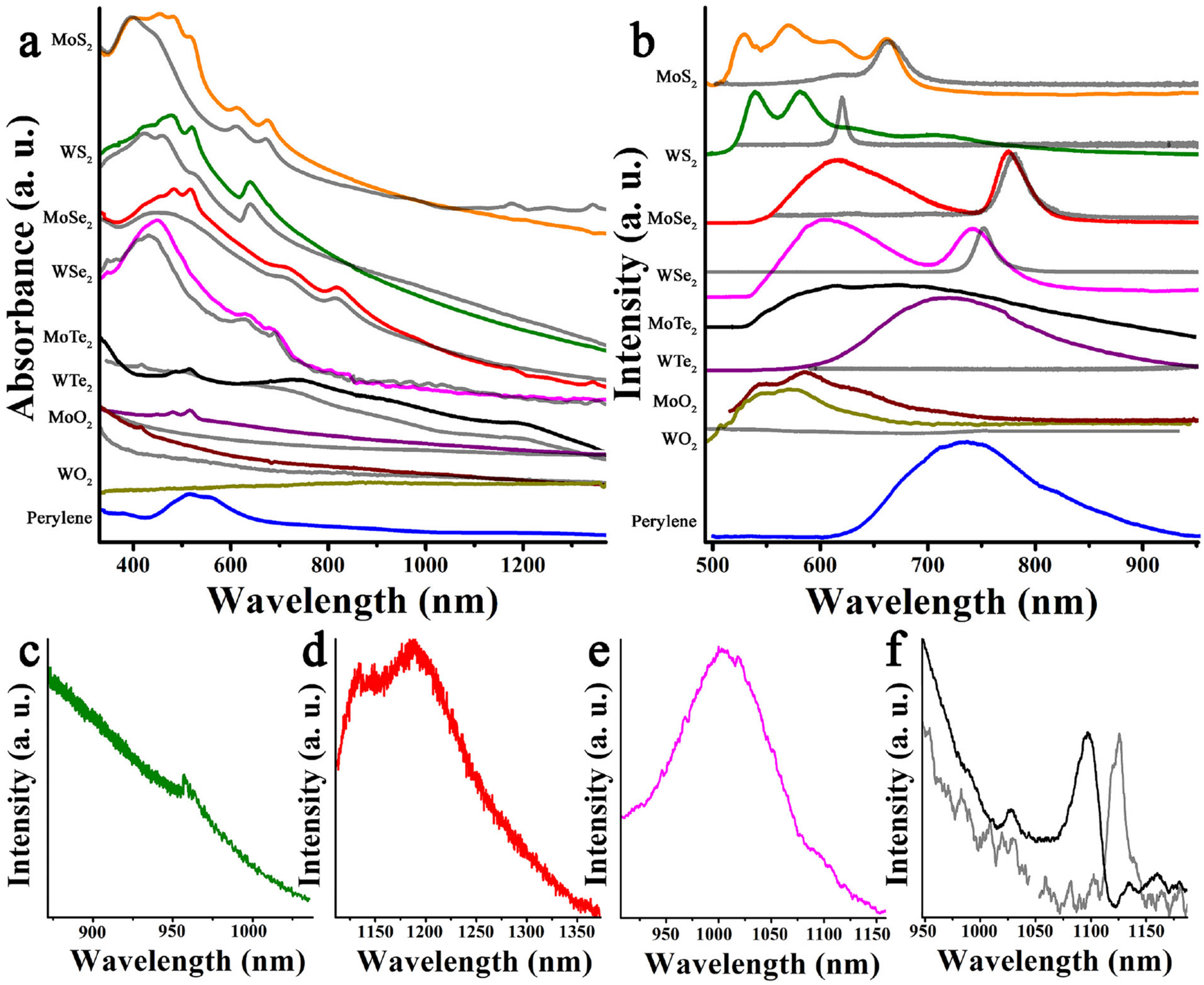

Fig. 5 (a) Absorption and (b) emission spectra (λ = 488 nm; 80 K) of TMDs: Per-MoS_2 (orange), Per-WS_2 (olive), Per-$MoSe_2$ (red), Per-WSe_2 (pink), Per-$MoTe_2$ (black), Per-WTe_2 (purple), Per-MoO_2 (wine), Per-WO_2 (dark yellow), and perylene (blue). The intensity of all materials has been normalized with pristine TMDs (gray) under the same conditions. Magnification of Near-IR emission bands of (c) Per-WS_2, (d) Per-$MoSe_2$, (e) Per-WSe_2 and (f) pristine $MoTe_2$ (gray) and Per-$MoTe_2$ (black).

These spectroscopic modifications suggest that in liquid states, perylenes are molecularly insolated, whereas in solid states, there is significant perylene–perylene aggregation. On the other hand, the perylene signatures within the hybrid materials were perfectly distinguishable, like free perylene in liquid media. For example, perylene bands appear at 457, 487, and 519 nm in Per-MoS_2, with a shift of ±3 nm in other hybrid materials. Conversely, the intensity of the TMDs signatures is slightly modified, whereas a global red shift has been observed. Specifically, all bands shift by 2–7 nm in MoS_2, 1–4 nm in WS_2, 2–8 nm in $MoSe_2$, and 1–7 nm in WSe_2. Only $MoTe_2$ displays a blue shift of its bands at 1205 nm, achieving a value of 1188 nm in Per-$MoTe_2$. These changes in the spectroscopic morphology indicate strong interactions between the orbitals of perylene and TMDs.[56,59,60,63]

2.4.2 **Emission.** The PL emission of solid Perylene aggregates is broad, extending from 650 to 850 nm, with a maximum at 732 nm (1.70 eV). This contrasts sharply with isolated perylenes, which exhibit emission at 550 nm (2.26 eV) in liquid conditions, where π–π interactions are suppressed.[59] The solid-state PL emission of the hybrid materials exhibits a perylene signature similar to that of isolated perylenes, with emission bands appearing between 530 and 615 nm (1.96 to 2.35 eV). More specifically, Per-MoS_2 exhibits three perylene emission bands at 529, 571, and 611 nm (2.34, 2.17, and 2.03 eV), forming a mirror image of its UV-Vis absorption spectrum. Per-WS_2, Per-MoO_2, and Per-WO_2 show similar signatures, with negligible shifts. Conversely, the signatures of Per-$MoSe_2$ and Per-WSe_2 are slightly shifted and broadened, with peaks at 585, 616, and 666 nm (2.12, 2.01, and 1.86 eV), indicating partial perylene-perylene interactions. These interactions are moderate in Per-$MoTe_2$ and pronounced in Per-WTe_2. Fig. 5b–f displays a representative spectrum of each material, extracted between 10–100 Kelvin, whereas Fig. S3† provides the full spectra across the entire temperature range. By employing the Varshni equation (see eqn (S1)†), the TMDs band gap of Per-MoS_2, Per-WS_2, Per-$MoSe_2$, Per-WSe_2 was calculated to be 1.91, 2.04, 1.60 and 1.71 eV, respectively.

The PL emission associated with the semiconducting properties of TMDs sharply decreases after functionalization with perylene. Starting with pristine materials, the signatures of MoS_2, WS_2, $MoSe_2$, WSe_2 and $MoTe_2$ are shown at 664, 620, 779, 752 and 1125 nm (1.87, 2.00, 1.59, 1.65 and 1.1 eV), respectively. Following functionalization, emission peaks were recorded at 661, 622, 775, 742, and 1097 nm (1.88, 1.99, 1.59, 1.67, and 1.13 eV) for Per-MoS_2, Per-WS_2, Per-$MoSe_2$, Per-WSe_2, and Per-$MoTe_2$, in the same order.[54] At low temperatures, several excitonic species, including neutral excitons, trions, and biexcitons, can typically be distinguished, influenced not only by temperature but also by incident power. Although these signatures are recorded in pristine materials, the spectral morphology remains invariant in the hybrid materials, probably due to the interaction with perylene. More interesting, Per-WS_2, Per-$MoSe_2$, and Per-WSe_2 (Fig. 5c–e) exhibit an additional band at lower energies after functionalization, at 957, 1189, and 1006 nm (1.30, 1.04, and 1.23 eV), respectively, which is likely related to electron–hole recombination between the perylenes and TMDs.[54] This band saturates at high power densities, showing $\alpha < 1$, as expected due to the relatively small loading of perylenes. A representative example of the power dependence of Per-WS_2 is provided in the ESI (Fig. S4a and b†).

Next, measuring the lifetimes of the hybrid materials proved challenging due to significant quenching effects from perylene.[90] Nonetheless, it is important to note that all pristine materials typically exhibited lifetimes shorter than 0.1 ns.[54] Perylene exhibited a lifetime of 3 ns, while the overall lifetime of Per-$MoSe_2$ decreased to 0.5 ns, resulting in an ultrafast decay in other materials that could not be accurately measured with our instrument (see Fig. S4c†). This reduction in lifetime might be related to electron–hole or energy transfer between perylenes and TMDs.

Further, photoluminescence excitation (PLE) assays performed on Per-MoS_2, Per-WS_2, Per-$MoSe_2$ and Per-WSe_2 exhibit maximum intensity between 500–600 nm, following the same pattern as the absorption spectrum of perylene (see Fig. S5†). Conclusively, in the particular configuration presented in this contribution, signatures of perylene were recorded as isolated species, which tend to block the intrinsic fluorescence properties of all TMDs.

2.5 Electrochemical properties

Electrochemical assays are of great interest as they offer insights into the reductive and oxidative potentials of each species, providing a fundamental basis for understanding the electronic interactions between perylenes and TMDs. Firstly, the square wave voltammetry (SWV) in Fig. 6a shows the first oxidative and reductive potentials of perylene at 1.27 and −0.94 V corresponding‡ to LUMO and HOMO values of −3.86 and −6.07 eV, respectively, in the energy vacuum diagram, assuming a Fermi level of −4.8 eV for ferrocene (Fc/Fc^+). The interpretation of TMDs is more complex. For example, MoS_2 and $MoSe_2$ exhibit first oxidation potentials at 0.3 V and 0.08 V, respectively, which do not correspond to the valence band maximum (VBM) but rather to defective regions of the material.[53] Similar behavior has been observed in WS_2 and WSe_2, with oxidation potentials recorded at 0.04 V and 0.09 V,

---

‡ Electrochemistry may be considered controversial for evaluating the positions of energy gaps in materials. The primary reason for this is that during oxidative or reductive processes, the material could undergo chemical changes that modify its electronic states. However, it is well known that perylenes and TMDs are chemically stable under oxidative or reductive potentials, suggesting that the current methodology is applicable.

Cyclic voltammetry, therefore, might not be suitable for evaluating novel materials. However, since our system involves the interaction of two well-known and chemically stable materials (TMDs and perylenes), simple math calculations should suffice to verify whether the oxidative or reductive positions align with the values reported in the literature. This approach acknowledges the limitations of the system while providing reliable results. Additionally, the HOMO and LUMO gaps of perylene align well with its optical gap, while the conduction and valence bands of the TMDs correspond closely to the gaps calculated using the Varshni eqn (S1).†

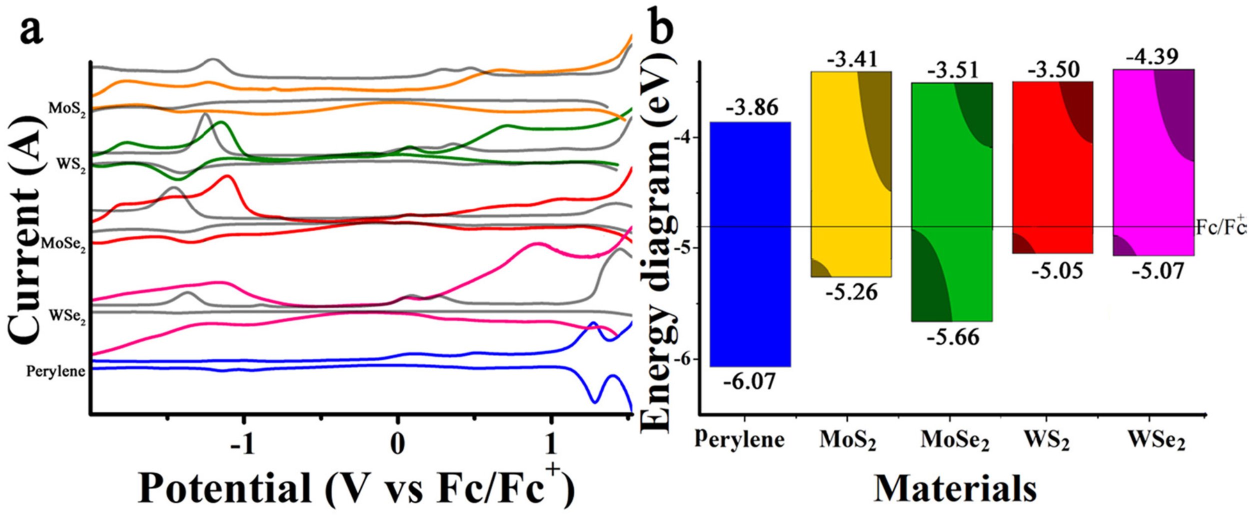

Fig. 6 (a) SWV of Per-MoS_2 (orange), Per-WS_2 (olive), Per-$MoSe_2$ (red), Per-WSe_2 (pink), Per-$MoTe_2$ (black), Per-WTe_2 (purple), Per-MoO_2 (wine), Per-WO_2 (dark yellow), and perylene at 514 nm (blue). All materials have been normalized with pristine TMDs (gray) under the same conditions in dry and deoxygenated acetonitrile, with 0.1 M of tetrabutylammonium hexafluorophosphate. (b) Electrochemical energy vacuum diagram.

respectively.[91,92] These short peaks are not related to the VBM but are instead associated with trap states, which may also be relevant for explaining the electronic processes involved in the interaction with perylene. The VBM for MoS_2, $MoSe_2$, WS_2, and WSe_2 are associated with oxidation potentials of 0.46, 0.25, 0.86 and 0.27 V, showing values of −5.26, −5.05, −5.66 and −5.07 eV. Similarly, the conduction band minimum (CBM) for MoS_2, $MoSe_2$, WS_2, and WSe_2 corresponds to the reductive potentials at −1.39, −1.30, −1.40, and −1.41 V, yielding energy values of −3.41, −3.50, −3.51, and −3.39 eV, respectively.[54,91,92] Table 1 shows the most relevant oxidation and reduction peaks for perylene, MoS_2, $MoSe_2$, WS_2 and WSe_2. Regarding Per-MoS_2, Per-$MoSe_2$, Per-WS_2 and Per-$MoSe_2$ the reduction and oxidation peaks related with the CBM and VBM of the TMDs or perylene exhibit minimal variation, less than ±0.2 V. Additionally, electrochemical bands associated with trap states were significantly reduced in the hybrid materials, suggesting that the inclusion of perylene effectively passivates these energetic states.[93] Notably, the new emissive bands observed in WS_2, $MoSe_2$, and WSe_2 at 1.30, 1.04, and 1.23 eV, respectively, align well with the differences between the redox reduction potential of perylene at −0.94 V and the trap states of WS_2, $MoSe_2$, and WSe_2 at 0.36, 0.08, and 0.27 V, resulting in electrochemical gaps of 1.30, 1.02, and 1.21 eV. This suggests that the presence of these new bands corresponds to electron–hole pairs formed between perylene and the TMDs (see Fig. S6a†).

Through the integration of optical and electrochemical data, an orbital diagram, depicted in Fig. 6b, may be constructed to elucidate the behavior of the photodevices. Before proceeding, it is important to highlight for readers with a background in physics or related fields that our nomenclature might be puzzling, as perylene behaves as a molecule with distinct molecular orbitals, while the TMDs possess energy bands, resulting in a hybrid system of mixed orbitals and bands. Having established this premise, the explanation begins by noting that the HOMO and LUMO levels of perylene are deeper than the VBM and CBM of the TMDs, leading to a type II alignment for MoS_2, WS_2, $MoSe_2$, and WSe_2. Given that the electrochemical assays reveal a significant number of hole-trap states, the TMDs materials contain energy states below the LUMO of perylene, causing the system to behave like a pseudo-type I alignment. Specifically, under dark conditions, spontaneously generated electrons in the CBM in the TMDs

Table 1 Oxidative and reductive potentials *via* sweep pulse voltammetry

Material	Oxidation (V)				Reduction (V)				HOMO (eV)	LUMO (eV)	GAP (eV)
Perylene		1.27			−0.94	−1.139	−2.3	0.94	−6.07	−3.86	2.21
MoS_2	0.3	0.46	1.51		−1.39	−2.1			−5.26	−3.41	1.85
$MoSe_2$	0.08	0.25	1.41		−1.3				−5.05	−3.5	1.55
WS_2	0.04	0.16	0.36	0.86	−1.4	−1.29	−2.11	0.04	−5.66	−3.51	2.15
WSe_2	0.09	0.27	1.45		−1.41				−5.07	−3.39	1.68
Per-MoS_2		0.47	0.66	1.31	−0.86	−1.41			−5.46	−3.94	1.52
Per-$MoSe_2$	0.08	0.73	1.06	1.21	−0.917	−1.339			−4.88	−3.883	1.0
Per-WS_2		0.07	0.71	1.001	−0.82	−1.426	−1.91		−5.51	−3.374	2.14
Per-WSe_2		0.055	0.913	1.22	−0.96	−1.52			−4.855	−3.84	1.02

can transfer to the LUMO of perylene, depleting the number of carriers, while spontaneously generated electrons in the LUMO and holes in the HOMO of perylene may transfer to trap states near the conduction or valence bands of TMDs (see an example in see Fig. S6b and c†). Under light illumination, however, the number of holes transferred from the HOMO of perylene might saturate the surrounding trap states, thereby increasing the population of holes in the valence band and consequently enhancing conductivity or carrier mobility (see Fig. S6d†). The electrons excited to the LUMO of perylene by the light do not have enough energy to reach the conduction band of MoS_2, WS_2, $MoSe_2$, or WSe_2, but they might contribute to saturating a significant portion of the TMDs hole trap states. As a result, the photogenerated electrons in the conduction band of the TMDs will not be easily trapped, leading to increased carrier mobility. Finally, due to the large band gap of perylene, energy transfer is also plausible. Under these circumstances, a photon absorbed by perylene may excite an electron from the valence band or trap states of the TMDs to their conduction band or trap states, resulting in conditions similar to those expected in a type I alignment (see Fig. S6e†).

In summary, under dark conditions, perylene has a minimal effect on the valence band of TMDs due to the presence of trap states (see Fig. S6c†). However, it negatively affects the conduction band in the TMDs hybrids, leading to a reduction in electron mobility (see Fig. S6b†). Under light illumination, perylene may inject hole carriers into the TMDs through ground-state interactions, while the negative effects observed in the excited states are significantly diminished or even reversed (see Fig. S6d†).

2.6 Devices properties

2.6.1 Phototransistor. 3-Terminal devices with a FET configuration were fabricated by contacting a single layer of semiconducting TMDs, grown *via* CVD, with Bi/Au electrodes (20 nm/50 nm) through metal deposition on a SiO_2 substrate with a thickness of 270 nm. The devices featured a channel length of 5 μm targeting monocrystalline single layers of MoS_2, WS_2, $MoSe_2$, and WSe_2, while $MoTe_2$ was polycrystalline. For WTe_2, a few-layered nanofilm was used. Regarding MoO_2 and WO_2, the channel contains nanomaterial flakes with thicknesses of 15 nm and 50 nm, respectively (see Fig. S7†). The same TMDs-based devices were measured under identical conditions, both before and after functionalization with perylene (see Fig. 7a). While replicating the exact conditions for the last three materials proved challenging, all parameters were meticulously standardized to ensure comparability with our prior research based on the functionalization of TMDs with PCBM.[54] A brief comparison is provided later.

First, the conductivity of the materials significantly decreases after functionalization, with Per-MoS_2, Per-WS_2, Per-$MoSe_2$, Per-WSe_2, Per-MoO_2, and Per-WO_2 showing 1000-, 100-, 50-, 40-, 10-, and 10 000-fold reductions, respectively, compared to the pristine materials under dark conditions (see Fig. 7b–i). This phenomenon is consistent with the discussion in section 5 and Fig. S6b and c,† which explains how perylene reduces the number of available carriers in the TMDs. Although low conductivity can present challenges in various systems, the signal-to-noise ratio remains unaffected, making these materials still of great interest for the fabrication of photodetectors and other nanotechnology applications. Interestingly, the dark current of Per-$MoTe_2$ increases by approximately 10-fold (see Fig. 7f). Despite being unable to evaluate the energy levels *via* electrochemistry, the literature indicates that the valence band of $MoTe_2$ is at 4.9 eV (*via* UPS)[94] with a bandgap of 1.1 eV. Therefore, the conduction band is estimated to be at approximately −3.8 eV,[95] which is close to the LUMO of perylene, suggesting a type I alignment. Consequently, the previously described negative impact of perylene on the conduction band is mitigated, leading to enhanced conductivity (see Fig. S6f†).

Under light illumination at 532 nm, the photo-response of Per-MoS_2 increases more than 1000-fold compared to pristine MoS_2 (see Fig. 7b). This indicates that hole transfer from the HOMO of perylene substantially covers the hole trap states of MoS_2, significantly increasing the charge carrier density (see Fig. S6d†). Outside the excitation range, perylene does not significantly inject carriers to MoS_2 (see Fig. S6b and c†), reducing the enhancement of the photo-response (*e.g.*, only a 0.2-fold increase at 254 nm). A similar effect is observed in Per-$MoSe_2$ and Per-WSe_2, with improvements in photo-response by 33 and 150-fold at 532 nm, respectively, compared to pristine $MoSe_2$ and WSe_2 (see Fig. 7d and e).

The photo-response of Per-WS_2 (see Fig. 7c) under perylene excitation (at 405 nm or 532 nm) decreases by 20% compared to pristine WS_2, suggesting that the LUMO of perylene can efficiently recombines with holes in the VBM or nearby trap states (see Fig. S6a†). The recombination between the trap states, below CBM of WS_2 and HOMO of perylene likely results in the emission of a new band recorded at 1.30 eV (see Fig. 5c). However, the photo-response of Per-WS_2 increases outside the perylene excitation range. Specifically, at 650 nm, the photo-response of Per-WS_2 enhances 28-fold compared to pristine WS_2. This complex effect likely involves multiple factors, one significant possibility being that perylene is directly excited to the trap states in the conduction band of WS_2, allowing holes in perylene to transfer to the valence band of WS_2, thereby enhancing the system's conductivity (see Fig. S6g†).

Regarding Per-$MoTe_2$, the material exhibits a clear enhancement of its photo-response compared to pristine $MoTe_2$ (see Fig. 7f). Per-$MoTe_2$ shows small but consistent photo-responses outside the perylene regions, with slight magnification at 532 nm and 407 nm when perylene is irradiated. This behavior is consistent with a type I alignment, where perylene acts as an antenna, enhancing the photo-response throughout the entire spectral region analyzed in this study (see Fig. S6f†). Lastly, some intriguing effects have been observed with intrinsically metallic materials, that typically exhibit negligible or no photo-response in their pristine forms. Per-WTe_2 (see Fig. 7g) shows a negative photo-response, particularly under perylene excitation, with decreases of 90% at 532 nm and 25% at

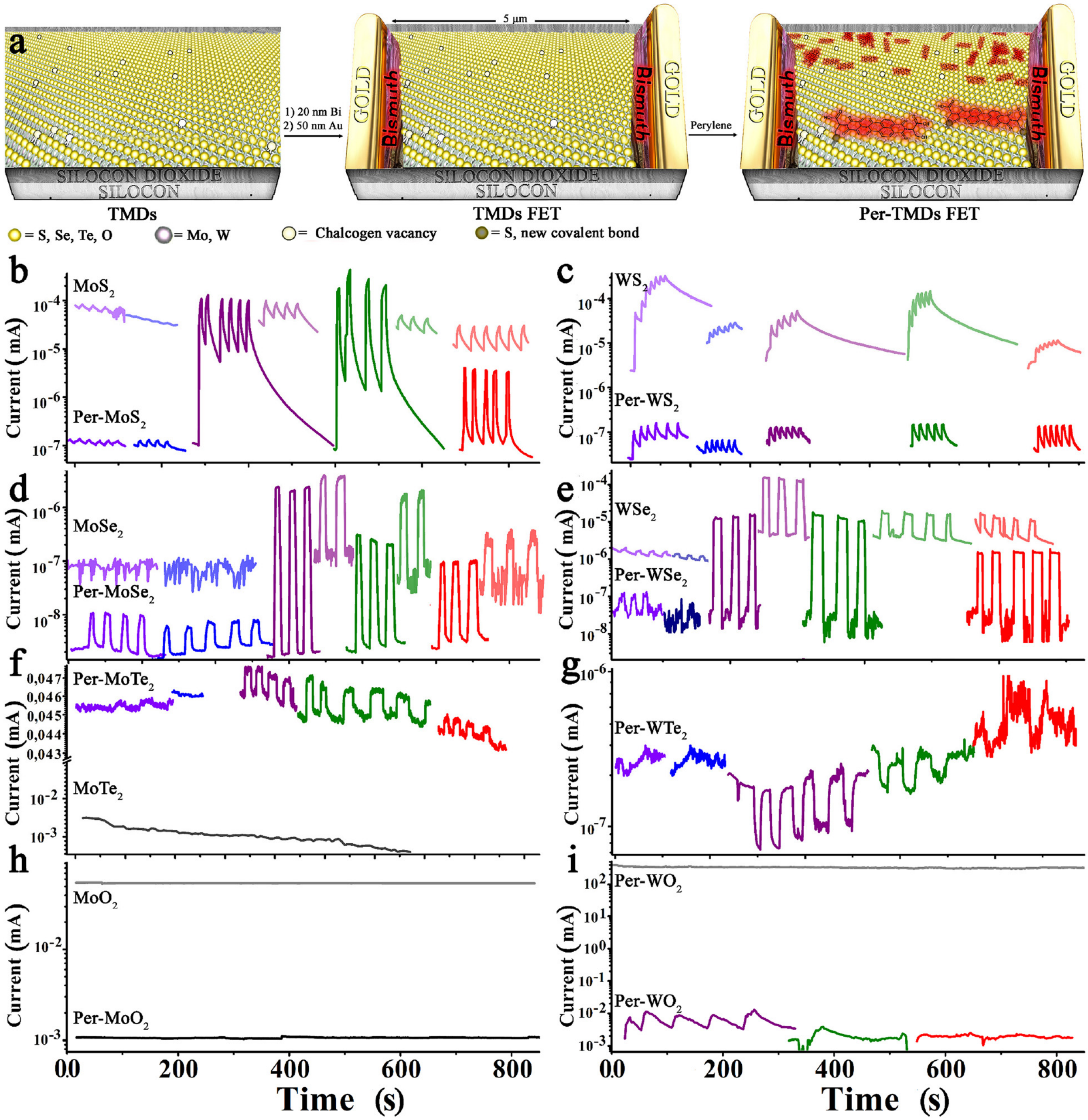

Fig. 7 (a) Fabrication of Per-TMDs-based phototransistors. Photo-response wavelength dependence for (b) Per-MoS$_2$ (opaque line) and pristine MoS$_2$ (semitransparent line), (c) Per-WS$_2$ (opaque line) and pristine WS$_2$ (semitransparent line), (d) Per-MoSe$_2$ (opaque line) and pristine MoSe$_2$ (semitransparent line), (e) Per-WSe$_2$ (opaque line) and pristine WSe$_2$ (semitransparent line), (f) Per-MoTe$_2$ (opaque line) and pristine MoTe$_2$ (semitransparent line), (g) Per-WTe$_2$ (opaque line) and pristine WTe$_2$ (semitransparent line), (h) Per-MoO$_2$ (opaque line) and pristine MoO$_2$ (semitransparent line), and (i) Per-WO$_2$ (opaque line) and pristine WO$_2$ (semitransparent line) at 254 (violet), 365 (blue), 407(purple), 532 (green), and 650 nm (red) light excitation pulses of 5 s and V_{D-S} of 1 V. The power intensity for 254 nm, 365 nm, 407 nm, 532 nm and 650 nm were 10 mW cm^{-2}, 10 mW cm^{-2}, 30 mW cm^{-2}, 17 mW cm^{-2} and 7 mW cm^{-2}.

650 nm. This effect is likely due to the trapping of holes and/or electrons by perylene, which reduces the conductivity in the hybrid material. In contrast, the photo-response of Per-WO$_2$ increases 8-fold at 407 nm compared to the pristine material (refer to Fig. 7i), suggesting the injection of electrons or holes into the system. Finally, metallic MoO$_2$ remains insensitive to light after functionalization with perylene (see Fig. 7h).

The recovery time after a light pulse is ultrafast in MoSe$_2$, WSe$_2$, MoTe$_2$, and WTe$_2$, making it challenging to accurately measure with our instruments. After functionalization, this ultrafast response is preserved, ensuring the good performance of the system. Conversely, the recovery time for pristine MoS$_2$ and WS$_2$ was critically slow, fitting well with a biexponential function. We observed fast recovery components with values of

1.0 and 21 seconds, and slow components of 31 and 165 seconds for MoS_2 and WS_2, respectively. The slow recovery components are attributed to trap states and defects that hinder rapid relaxation. After functionalization, the recovery times are partially shortened due to the trap state passivation by perylene, resulting in recovery times of 1 and 16 seconds for Per-MoS_2, and 1 and 13 seconds for Per-WS_2, respectively.[34,55,56] A representative fitting for Per-MoS_2 is included in the ESI as Fig. S8.† Although this is not our primary focus, such long-time recovery times are of interest for applications in neurological memory photodevices.

Based on factors such as incident light wavelength, laser power, channel dimensions, and applied voltage, several key parameters were calculated, including photo-response, responsivity, external quantum efficiency (EQE), specific detectivity (D^*), superficial conductivity (σ_{sq}), transconductance (G_m), and carrier mobilities (see eqn (S2)–(S8)†). This manuscript summarizes the best performance of the hybrid materials in Fig. 9, while comprehensive results are detailed in the ESI (Tables S2–7†). Optimal results were consistently achieved under 532 nm laser irradiation, with the highest photo-responses observed for Per-WSe_2 and Per-$MoSe_2$, with values of 3.9 × 10^5% and 2.6 × 10^5% each. The best responsivity and EQE were recorded for Per-$MoSe_2$ and Per-$MoTe_2$, with values of 4.6 and 26 A W^{-1}, and 1.1 × 10^3 and 6.1 × 10^3%, respectively. The greatest specific detectivity was obtained for Per-MoS_2, followed by Per-WSe_2 and Per-$MoSe_2$, with values of 1.1 × 10^{12}, 1.0 × 10^{11}, and 2.8 × 10^{10} Jones, respectively. Additionally, the highest transconductance and carrier mobilities were also achieved in Per-MoS_2, with values of 9.0 μA V^{-1} and 92.3 cm^2 V^{-1} s^{-1} respectively. The best superficial conductivity was observed in the metallic material Per-MoO_2 with a value of 3.4 × 10^{-3} S sq^{-1}, while among the semiconducting materials, Per-$MoTe_2$ showed the highest conductivity at 5.8 × 10^{-6} S sq^{-1}, followed by Per-MoS_2 at 3.9 × 10^{-8} S sq^{-1}. Volumetric conductivity, commonly expressed in S m^{-1}, is often incorrectly applied to 2D materials. In our data, this would suggest an improvement of more than 10^9-fold, which renders direct comparisons invalid and should be avoided. Therefore, the Per-MoS_2 device appears to be the most effective across the majority of analyses.

2.6.2 Transfer curves and output characteristics. Other relevant parameters commonly evaluated in FET transistors include transfer curves and output characteristics. Specifically, transfer curves were fundamental in determining the carrier mobility discussed in section 6.1. A representative example illustrating the performance of MoS_2 is provided in Fig. 8, while data for the other materials are included in ESI, Fig. S9.†

Firstly, under dark conditions, the transfer curves of MoS_2 exhibit n-type semiconductor characteristics with on–off ratios spanning six orders of magnitude, a behavior that is retained in Per-MoS_2 (Fig. 8a and b). Notably, this ratio becomes more pronounced following functionalization, sharply increasing from 40 V to 60 V, in contrast to the pristine material, where the current increases over the range of −60 V to 60 V. Additionally, at negative voltages ranging from −40 to −80 V, Per-MoS_2 demonstrates enhanced conductivity compared to pristine material, likely due to hole injection into the valence band by perylene. Under light irradiation, carrier injection increases the current across all wavelengths, with the effect being most pronounced in the perylene region, at 407 and 532 nm.

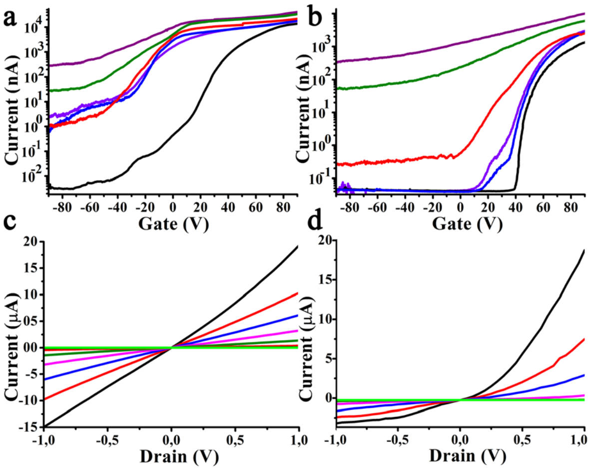

Fig. 8 Transfer curve of (a) pristine MoS_2 and (b) Per-MoS_2 at dark and at 254 (violet), 365 (blue), 407(purple), 532 (green), and 650 nm (red) light excitation. Output characteristics of (c) pristine MoS_2 and (b) Per-MoS_2 at different gate voltage, 80 V (black), 70 V (red), 60 V (blue), 50 V (pink), 40 V (olive), 30 V (red), 20 V or less (green). The V_{D-S} was 1 V. The power intensity for 254 nm, 365 nm, 407 nm, 532 nm and 650 nm were 10 mW cm^{-2}, 10 mW cm^{-2}, 30 mW cm^{-2}, 17 mW cm^{-2} and 7 mW cm^{-2}.

WS_2 and Per-WS_2 display on–off current ratios of 4 and 3 orders of magnitude, respectively, similar to WSe_2 and Per-WSe_2, while maintaining an n-type character. Per-$MoSe_2$ exhibits an on–off ratio with one-order-of-magnitude improvement after functionalization, revealing a p-type semiconductor character. Upon light irradiation, Per-WS_2, Per-WSe_2, and Per-$MoSe_2$ exhibit a similar effect to Per-MoS_2, with carrier injection enhancing the current throughout the system. For Per-$MoTe_2$, Per-WTe_2 and Per-WO_2, the drain-to-source ($V_{D\text{-}S}$) current remains stable across a range of gate voltages (V_G), indicating that these devices are better characterized as robust photodetectors rather than phototransistors.

Finally, the output characteristics in Fig. 8c and d reveal an asymmetry in the current flow for Per-MoS_2 compared to pristine MoS_2, indicating inhomogeneities caused by the presence of perylene.[54,55] An asymmetry in the output characteristics should not be mistaken for a drawback. In fact, it is quite the opposite. The larger conductivity at positive voltages, which is also photoactive, is characteristic of photodiodes. Thus, Per-MoS_2 can function not only as a phototransistor but also as a photodiode, meaning that the current passing through the system can be modulated not only by the gate voltage but also by its direction and light exposure, further enhancing its potential as a nanodevice. The examined voltage range shows no current saturation, confirming that the devices can operate effectively across a broad window of drain-to-source voltages, both positive and negative, while demonstrating a strong response to gate voltage. A similar effect is observed in Per-WS_2, Per-$MoSe_2$, and Per-WSe_2. In contrast, $MoTe_2$, WTe_2, MoO_2, and WO_2 exhibit no significant changes with gate voltage variation, exhibiting symmetry in both positive and negative voltages, thereby confirming bidirectional drain-to-source current behavior.

2.6.3 Comparative analysis within the framework of advanced tmds photodevices. Certainly, extensive research has focused on functionalizing TMDs for the fabrication of ultra-small photodevices, especially phototransistors. The 0D–2D structures hold particular interest for this area of nanotechnology.[31] For instance, PbS quantum dots on MoS_2 exhibits the best performance to our knowledge, with a remarkable photo-responsivity of 2×10^6 A W^{-1}.[96] The highest reported value for 1D/2D structures is found in 1D Te/2D $MoTe_2$,[97] which is two orders of magnitude lower, similar to the 3D/2D hybridization between MoS_2 and GaN.[98]

Close to this level of performance are organic–inorganic hybrids, MoS_2 functionalized non-covalently with perylene (MoS_2/perylene) standing out due to its highest photo-responsivity of 1×10^3 A W^{-1} and an impressive photo-response of 1.5×10^4%,[99] followed closely by MoS_2 functionalized with zinc-phthalocyanine (MoS_2/ZnPc),[34] which shows values of 4.3×10^2 A W^{-1} and 3.0×10^5%. A brief reminder is that the highest responsivity in this contribution is achieved with Per-$MoTe_2$, while Per-WSe_2 exhibits the most significant photo-response, with values of 26 A W^{-1} and 3.9×10^5%, respectively. However, the study of covalent functionalization with organic chromophores in this context remains largely unexplored. As mentioned previously, covalent functionalization facilitates thorough material cleaning and isolates individual molecules. Additionally, it prevents electron diffusion in organic-organic systems caused by aggregation, thereby enhancing performance. However, only a few contributions have targeted devices using this approach.

On the other hand, the performance of the devices depends on a wide range of factors, including the substrate,[6] the synthesis of the TMDs and the functionalization techniques,[18] challenging an accurate comparison. Said that, we previously functionalized TMDs with a PCBM derivative,[54] by employing not only the same conditions but even a piece of same CVD pristine TMDs substrate, which was divided into different fractions. Both PCBM and perylene were functionalized with cysteine, which enables covalent interaction with TMDs *via* thiol groups. The reactions with TMDs were conducted in parallel under identical conditions, resulting in sibling materials that allow for the best possible comparison. In fact, the best photo-response, responsivity, and detectivity performance of Per-TMDs were compared with PCBM-TMDs in Fig. 9. Although detectivity decreases when comparing each TMDs with its homologue, the responsivity remains comparable, and the photo-response is superior in Per-TMDs.

PCBM exhibited a similar alignment to perylene across most materials, except for MoS_2, where PCBM forms type I alignment in contrast with perylene, that forms a type II alignment. As a result, the conductivity of PCBM-MoS_2 increases, but its photo-response is two orders of magnitude smaller than that of Per-MoS_2. In contrast, Per-$MoTe_2$ exhibits a 50-fold increase in both responsivity and conductivity compared to PCBM-$MoTe_2$, at 532 nm. For other TMDs hybrid materials, perylene and PCBM show similar behavior, with notable enhancements of 10-fold for Per-$MoSe_2$ and 5-fold for Per-WSe_2 at 532 nm. However, the most significant difference lies in the photo-response outside this wavelength range. Perylene exhibits strong absorption between 450 and 600 nm, tailoring the photo-response primarily within this range, which is a desirable property for selective photo-devices. In contrast, PCBM displays a broader absorption spectrum, leading to an overall enhancement of photo-response across the visible spectrum, making it more suitable for non-selective photo-devices.

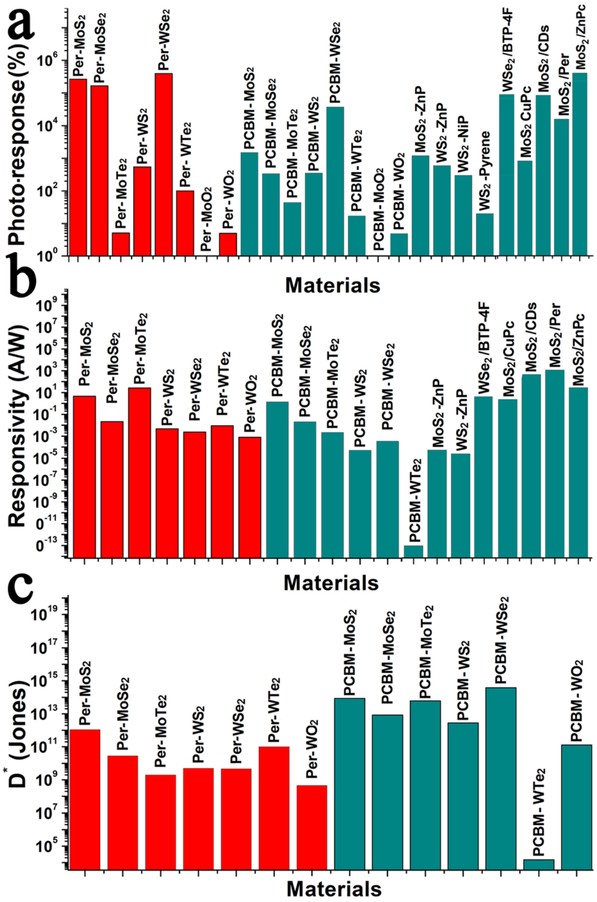

Fig. 9 Comparison of (a) photo-response, (b) responsivity, and (c) detectivity of Per-TMDs with PCBM-TMDs and other relevant studies.[34,36,54–56,61,99,100,101]

Experiments performed under covalent functionalization of ZnP with MoS_2 (ZnP-MoS_2) and WS_2 (ZnP-WS_2) were conducted under similar conditions.[54] However, a key difference was that the MoS_2 and WS_2 nanosheets were directly transferred onto a gold electrode, forming a Schottky barrier that hindered optimal performance. Focusing solely on the photo-response, ZnP-MoS_2 and ZnP-WS_2 exhibited values of 1200% and 600% under 405 nm laser irradiation. In contrast, their homologues, Per-MoS_2 and Per-WS_2, reached values of 96300% and 442%, respectively, with orbital alignment being the primary factor responsible for the differences observed between MoS_2 and WS_2. Specifically, ZnP acts as an electron donor, whereas PCBM and perylenes function as electron acceptors. WS_2 covalently functionalized with pyrene (WS_2-pyrene) generally shows worse results than our materials.[56] However, a direct comparison is not applicable, as those experiments were conducted on nanofilms rather than on a single WS_2 layer.

For instance, considering non-covalent functionalization with perylene, not under its best performance but under conditions comparable to our experiments—namely, power densities of 12.5 or 25 mW cm^{-2}, 5s pulses of 532 nm laser illumination, V_{DS} = 3 V, and V_G = 0 V—the reported photo-response is approximately 10-fold.[99] In contrast, our results show an enhancement of 2630-fold, at 17 mW cm^{-2} and V_{DS} = 1 V. A plausible explanation is that, in our system, perylene–perylene interactions are minimized, suppressing competitive charge transfer pathways that would otherwise reduce carrier mobility. Additionally, the responsivity of non-covalent MoS_2/perylene falls below 1 A W^{-1}. Similarly, the responsivity of MoS_2/ZnPc,[34] drops to 8 A W^{-1} under 532 nm illumination at 1.0 V and 3 mW cm^{-2} when V_G = 0 V. These values are comparable to those obtained for Per-MoS_2 and Per-$MoTe_2$, which exhibit responsivities of 4.6 and 26.2 A W^{-1}, respectively, at 17 mW cm^{-2}.

Without any additional in-depth analysis, Per-MoS_2, Per-MoS_2, and Per-WSe_2 exhibit a better photo-response than MoS_2 functionalized with Cu-phthalocyanine (MoS_2/CuPc)[36] or with CDs (MoS_2/CDs),[100] or WSe_2 functionalized with BTP-4F (WSe_2/BTP-4F).[101] On the other hand, the responsivity of MoS_2/CDs[100] is higher but still close to Per-MoS_2 and Per-Te_2. Moreover, Per-MoS_2 and Per-Te_2 show better performance than MoS_2/CuPc[36] or WSe_2/BTP-4F[101] (see Fig. 9). It must be noted, however, that the photo-response and responsivity can be tuned by applying a gate voltage, potentially increasing the values. Nevertheless, this aspect was beyond the primary focus of this contribution, which aims to fully understand the electronic mechanisms involved between TMDs and isolated planar electron-acceptor molecules such as perylene.

Therefore, although a precise analysis is not feasible due to variations in experimental conditions, a comparison with literature reports under similar conditions reinforces the exceptional performance of our system.

3. Experimental

3.1. Synthesis

3.1.1. CVD synthesis. This procedure has been previously published.[54] As example, MoS_2 (or WS_2) 15 mg of MoO_3 (or WS_2) containing 15% of NaCl was deposited at the centre of an alumina boat (10 × 1.5 cm^2) with a height of 1.1 cm. The boats were put in a quartz tube with 3 cm in diameter. Argon gas was flowed with a flow rate of 113 ml min^{-1}, and MoO_3 was gradually heated up to 725 °C (780 °C) in 13 minutes. And then, Sulphur was also heated up to 210 °C in 10 minutes. All CVD parameters were kept constant for 30 additional minutes before a slow cooling down. All conditions can be described on Table S1.†

3.1.2. Synthesis of perylene (*N*,*N*′-bis-(L-cysteine)-3,4,9,10-perylene tetracarboxylic diimide). The synthesis followed a procedure previously described in the literature.[64,65] Briefly, 3,4,9,10-perylene tetracarboxylic acid dianhydride (PTCDA) (1 g, 1 equiv.), L-cysteine (0.7 g, 5 equiv.), and 100 mL of DMF were added to a Schlenk flask and heated at 120 °C overnight. After cooling, the reaction mixture was subjected to vacuum to remove the solvent. The resulting crude solid was powdered and washed multiple times with hot water, followed by methanol and acetone. To reduce the disulfide bonds formed during the reaction, the product was acidified with trifluoroacetic acid, and excess zinc powder was added over several hours. The excess zinc was removed by filtration through filter paper, and the pH was neutralized with sodium carbonate, causing perylene to precipitate. Finally, the material was washed with hot water to remove excess cysteine. Yields: 50% NMR: (8H, perylene) 8.5–7.5 ppm, multiplet; (4H, Cys α, thiol) 6.0–5.0 ppm, multiplet; (4H, Cys β) 3.25–2.75 ppm, multiplet, partially masked by solvent peaks. IR: COOH (Cys) stretch 1700–1800 cm^{-1}; O=C–N–C=O (perylene) 1600–1700 cm^{-1}. MALDI: ($C_{30}H_{16}N_2NaO_8S_2$) calculated: 619.02, 620.03, 621.02, 621.03; found: 619.346, 620.360, 621.360.

3.1.3. TMDs-Per. MoS_2 (or WS_2) or other TMDs on SiO_2/Si was immersed in 5 ml of DMAc with 1 mg of perylene-Cys. Pellets of Zn was added to prevent cysteine-cysteine dimerization of perylene, and the system was protected against light, oxygen or moisture. Reactions were kept under minimum stirring during 4 days *in vacuo* at 50 °C (40 °C) or room temperature and dark. Then, it was cleaned with pure DMAc four times by immersion. Lately, non-covalent spices were completely removed employing DMAc under Solhex reflux during 12 h.

Please refer to ESI† for instrumentation, methods and techniques.

4. Conclusions

In this contribution, perylene was successfully insolated on the surface of various single-layer TMDs through covalent functionalization. The materials underwent detailed characterization, followed by an in-depth analysis of their optical and electronic properties. Perylene forms a type II alignment with all semiconducting TMDs, except for $MoTe_2$, where a type I alignment is observed. However, trap states play a crucial role, causing all the hybrid materials to behave as if they exhibit a pseudo-type I alignment. The intrinsic PL emission of all the TMDs undergoes a significant reduction. In contrast, the light absorption is greatly enhanced in the perylene region (400–600 nm) in hybrid materials. Interestingly, the photo-response emerges immediately after functionalization in tungsten-based metallic materials, such as Per-WO_2, and improves in semiconducting materials, with a 1000-fold increase observed in Per-MoS_2 and Per-WSe_2 reaching values of 3.9×10^5% and 2.6×10^5%, respectively. The highest carrier mobility was achieved by Per-MoS_2, with a value of 92.3 $cm^2\ V^{-1}\ s^{-1}$, while the best responsivity was observed in Per-$MoTe_2$, reaching 26.2 $A\ W^{-1}$. The photo-response, responsivity, and specific detectivity values achieved through this study are comparable to the highest-performing systems involving non-covalent functionalization. This approach is both straightforward and effective, allowing for the precise integration of molecules onto TMDs surfaces while tailoring their properties. We demonstrate that perylene can uniquely modify each TMDs, and we discuss its potential target applications. Furthermore, we compare our results with those reported in the literature, confirming the outstanding performance of the Per-TMDs devices. As a result, this method holds significant potential for advancing applications in nanotechnology and energy conversion.

Data availability

The data supporting this article have been included as part of the ESI.†

Conflicts of interest

"There are no conflicts to declare".

Acknowledgements

This work was supported by the Grant-in-Aid for Scientific Research KAKENHI (21H05015, 22H01907, 23K17956), Japan Society for the Promotion of Science (JSPS), Design & Engineering by Joint Inverse Innovation for Materials Architecture (DEJI^{2}MA), MEXT and the joint usage/research program of IMaSS, Nagoya University. and from Japan Society for the Promotion of Science (JSPS) postdoctoral fellowship grant agreement No P19368.

References

1 W. Choi, N. Choudhary, G. H. Han, J. Park, D. Akinwande and Y. H. Lee, *Mater. Today*, 2017, **20**, 116–130, DOI: **10.1016/j.mattod.2016.10.002**.

2 N. Huo and G. Konstantatos, *Adv. Mater.*, 2018, **30**, 1801164, DOI: **10.1002/adma.201801164**.

3 B. Zhao, D. Shen, Z. Zhang, P. Lu, M. Hossain, J. Li, B. Li and X. Duan, *Adv. Funct. Mater.*, 2021, **31**(48), 2105132, DOI: **10.1002/adfm.202105132**.

4 R. C. Longo, R. Addou, K. C. Santos, J.-Y. Noh, C. M. Smyth, D. Barrera, C. Zhang, J. W. P. Hsu, R. M. Wallace and K. Cho, *2D Mater.*, 2017, **4**, 025050, DOI: **10.1088/2053-1583/aa636c**.

5 R. Canton-Vitoria, T. Hotta, Z. Liu, T. Inoue and R. Kitaura, *J. Chem. Phys.*, 2020, **153**, 084702, DOI: **10.1063/5.0012782**.

6 A. S. Aji, P. Solís-Fernández, H. G. Ji, K. Fukuda and H. Ago, *Adv. Funct. Mater.*, 2017, **27**(47), 1703448, DOI: **10.1002/adfm.201703448**.

7 A. Allain and A. Kis, *ACS Nano*, 2014, **8**(7), 7180–7185, DOI: **10.1021/nn5021538**.

8 Z. Yu, Y. Zhu, W. Li, Y. Shi, G. Zhang, Y. Chai and X. Wang, *2018 IEEE International Electron Devices Meeting (IEDM)*, 2018. DOI: **10.1109/IEDM.2018.8614644**.

9 S. Larentis, B. Fallahazad and E. Tutuc, *Appl. Phys. Lett.*, 2012, **101**, 223104, DOI: **10.1063/1.4768218**.

10 S. H. Mir and V. K. Yadav, *ACS Omega*, 2020, **5**(24), 14203–14211, DOI: **10.1021/acsomega.0c01676**.

11 Z. Zhao, F. Dong, Y. Wang, J. Sun, H. Ye, R. Wang and J. Zhang, *Nanoscale*, 2023, **15**, 11955–11962, DOI: **10.1039/D3NR00849E**.

12 A. Apte, K. Mozaffari, F. S. Samghabadi, J. A. Hachtel, L. Chang, S. Susarla, J. C. Idrobo, D. C. Moore, N. R. Glavin, D. Litvinov, P. Sharma, A. B. Puthirath and P. M. Ajayan, *Adv. Mater.*, 2020, **32**(24), 2000006, DOI: **10.1002/adma.202000006**.

13 J. Moosburger-Will, J. Kündel, M. Klemm, S. Horn, P. Hofmann, U. Schwingenschlögl and V. Eyert, *Phys. Rev. B: Condens. Matter Mater. Phys.*, 2009, **79**(11), 104113, DOI: **10.1103/physrevb.79.115113**.

14 R. Wu, J. Zhang, Y. Shi, D. Liu and B. Zhang, *J. Am. Chem. Soc.*, 2015, **137**(22), 6983–6986, DOI: **10.1021/jacs.5b01330**.

15 C. Lyu, L. Zhang, X. Zhang, H. Zhang, J. Xie, J. Zhang, Y. Liu, Y. Liu, R. Wu, J. Zhang, C. Zha, W. Wang, Z. Wan, B. Li, C. Zhu, H. Ma, X. Duan and L. Wang, *Adv. Mater.*, 2023, **35**(12), 2207895, DOI: **10.1002/adma.202207895**.

16 P.-C. Shen, C. Su, Y. Lin, A.-S. Chou, C.-C. Cheng, J.-H. Park, M.-H. Chiu, A.-Y. Lu, H.-L. Tang, M. M. Tavakoli, G. Pitner, X. Ji, Z. Cai, N. Mao, J. Wang, V. Tung, J. Li, J. Bokor, A. Zettl, C.-I. Wu, T. Palacios, L.-J. Li and J. Kong, *Nature*, 2021, **593**, 211–217, DOI: **10.1038/s41586-021-03472-9**.

17 J. Wang, H. Fang, X. Wang, X. Chen, W. Lu and W. Hu, *Small*, 2017, **13**, 1700894, DOI: **10.1002/smll.201700894**.

18 W. Zhao, Z. Ghorannevis, K. K. Amara, J. R. Pang, M. Toh, X. Zhang, C. Kloc, P. H. Tan and G. Eda, *Nanoscale*, 2013, **5**, 9677, DOI: **10.1039/C3NR03052K**.

19 C. Backes, B. M. Szydłowska, A. Harvey, S. Yuan, V. Vega-Mayoral, B. R. Davies, P. Zhao, D. Hanlon, E. J. G. Santos, M. I. Katsnelson, W. J. Blau, C. Gadermaier and J. N. Coleman, *ACS Nano*, 2016, **10**, 1589, DOI: **10.1021/acsnano.5b07228**.

20 C. Backes, R. J. Smith, N. McEvoy, N. C. Berner, D. McCloskey, H. C. Nerl, A. O'Neill, P. J. King, T. Higgins, D. Hanlon, N. Scheuschner, J. Maultzsch, L. Houben, G. S. Duesberg, J. F. Donegan, V. Nicolosi and

J. N. Coleman, *Nat. Commun.*, 2014, **5**, 4576, DOI: **10.1038/ncomms5576**.

21 K.-G. Zhou, M. Zhao, M.-J. Chang, Q. Wang, X.-Z. Wu, Y. Song and H.-L. Zhang, *Small*, 2014, **10**, 400541, DOI: **10.1002/smll.201400541**.

22 C.-H. Chang, X. Fan, S.-H. Lin and J.-L. Kuo, *Phys. Rev. B: Condens. Matter Mater. Phys.*, 2013, **88**, 195420, DOI: **10.1103/PhysRevB.88.195420**.

23 S. Zhang, M. Maruyama, S. Okada, M. Xue, K. Watanabe, T. Taniguchi, K. Hashimoto, Y. Miyata, R. Canton-Vitoria and R. Kitaura, *Nanoscale*, 2023, **15**, 5948–5953, DOI: **10.1039/D2NR06616E**.

24 Z. Lin, B. R. Carvalho, E. Kahn, R. Lv, R. Rao, H. Terrones, M. A. Pimenta and M. Terrones, *2D Mater.*, 2016, **3**, 022002, DOI: **10.1088/2053-1583/3/2/022002**.

25 S. Sahoo, A. P. Gaur, M. Ahmadi, M. J.-F. Guinel and R. S. Katiyar, *J. Phys. Chem. C*, 2013, **117**, 9042–9047, DOI: **10.1021/jp402509w**.

26 J. Quan, L. Linhart, M.-L. Lin, D. Lee, J. Zhu, C.-Y. Wang, W.-T. Hsu, J. Choi, J. Embley and C. Young, *Nat. Mater.*, 2021, **20**, 1100–1105, DOI: **10.1038/s41563-021-00960-1**.

27 X. Zhang, X.-F. Qiao, W. Shi, J.-B. Wu, D.-S. Jiang and P.-H. Tan, *Chem. Soc. Rev.*, 2015, **44**, 2757–2785, DOI: **10.1039/C4CS00282B**.

28 X. Yin, C. S. Tang, Y. Zheng, J. Gao, J. Wu, H. Zhang, M. Chhowalla, W. Chen and A. T. S. Wee, *Chem. Soc. Rev.*, 2021, **50**, 10087–10115, DOI: **10.1039/D1CS00236H**.

29 Q. Liang, Q. Zhang, X. Zhao, M. Liu and A. T. S. Wee, *ACS Nano*, 2021, **15**, 2165–2181, DOI: **10.1021/acsnano.0c09666**.

30 Y. Murai, S. Zhang, T. Hotta, Z. Liu, T. Endo, H. Shimizu, Y. Miyata, T. Irisawa, Y. Gao, M. Maruyama, S. Okada, H. Mogi, T. Sato, S. Yoshida, H. Shigekawa, T. Taniguchi, K. Watanabe, R. Canton-Vitoria and R. Kitaura, *ACS Nano*, 2021, **15**, 19225–19232, DOI: **10.1021/acsnano.1c04584**.

31 V. Selamneni and P. Sahatiya, *Microelectron. Eng.*, 2023, **269**, 111926, DOI: **10.1016/j.mee.2022.111926**.

32 H. Zhang, J. Choi, A. Ramani, D. Voiry, S. N. Natoli, M. Chhowalla and J. H. Choi, *ChemPhysChem*, 2016, **17**, 2854–2862, DOI: **10.1002/cphc.201600511**.

33 H. Zhang, J. Ji, A. A. Gonzalez and J. H. Choi, *J. Mater. Chem. C*, 2017, **5**, 11233–11238, DOI: **10.1039/c7tc02861j**.

34 Y. Huang, F. Zhuge, J. Hou, L. Lv, P. Luo, N. Zhou, L. Gan and T. Zhai, *ACS Nano*, 2018, **12**, 4062–4073, DOI: **10.1021/acsnano.8b02380**.

35 J. Choi, H. Zhang and J. H. Choi, *ACS Nano*, 2016, **10**, 1671–1680, DOI: **10.1021/acsnano.5b07457**.

36 J. Pak, J. Jang, K. Cho, T.-Y. Kim, J.-K. Kim, Y. Song and T. Lee, *Nanoscale*, 2015, **7**, 18780–18788, DOI: **10.1039/c5nr04836b**.

37 P. Sahatiya, S. S. Jones and S. Badhulika, *Appl. Mater. Today*, 2018, **10**, 106–114, DOI: **10.1016/j.apmt.2017.12.013**.

38 J. Baek, T. Umeyama, W. Choi, Y. Tsutsui, H. Yamada, S. Seki and H. Imahori, *Chem. – Eur. J.*, 2018, **24**, 1561–1572, DOI: **10.1002/chem.201703699**.

39 Y. Xing, Y. Wang, L. Liu and Z. Wu, *Micromachines*, 2023, **14**, 660, DOI: **10.3390/mi14030660**.

40 R. Canton-Vitoria, Y. Sayed-Ahmad-Baraza, B. Humbert, R. Arenal, C. Ewels and N. Tagmatarchis, *Nanomaterials*, 2020, **10**, 363, DOI: **10.3390/nano10020363**.

41 X. Liu, J. Gu, K. Ding, D. Fan, X. Hu, Y.-W. Tseng, Y.-H. Lee, V. Menon and S. R. Forrest, *Nano Lett.*, 2017, **17**, 3176–3181, DOI: **10.1021/acs.nanolett.7b00695**.

42 A. Stergiou, R. Canton-Vitoria, M. N. Psarrou, S. P. Economopoulos and N. Tagmatarchis, *Prog. Mater. Sci.*, 2020, **114**, 100683, DOI: **10.1016/j.pmatsci.2020.100683**.

43 G. Guan and M.-Y. Han, *Adv. Sci.*, 2019, **6**, 1901837, DOI: **10.1002/advs.201901837**.

44 X. Chen and A. R. McDonald, *Adv. Mater.*, 2016, **28**, 5738–5746, DOI: **10.1002/adma.201505345**.

45 A. Zhuravlova, A. G. Ricciardulli, D. Pakulski, A. Gorczyński, A. Kelly, J. N. Coleman, A. Ciesielski and P. Samorì, *Small*, 2023, **19**, 2208100, DOI: **10.1016/j.snb.2016.12.044**.

46 B. Xu, Y. Su, L. Li, R. Liu and Y. Lv, *Sens. Actuators, B*, 2017, **246**, 380–388, DOI: **10.1016/j.snb.2016.12.044**.

47 P. Behera, K. K. Singh, S. Pandit, D. Saha, D. K. Saini and M. De, *ACS Appl. Nano Mater.*, 2021, **4**, 3843–3851, DOI: **10.1021/acsanm.0c03827**.

48 R. Canton-Vitoria, C. Stangel and N. Tagmatarchis, *ACS Appl. Mater. Interfaces*, 2018, **10**, 23476–23480, DOI: **10.1021/acsami.8b08272**.

49 R. Canton-Vitoria, E. Istif, J. Hernández-Ferrer, E. Urriolabeitía, A. M. Benito, W. K. Maser and N. Tagmatarchis, *ACS Appl. Mater. Interfaces*, 2019, **11**, 5947–5956, DOI: **10.1021/acsami.8b18435**.

50 R. Canton-Vitoria, L. Vallan, E. Urriolabeitia, A. M. Benito, W. K. Maser and N. Tagmatarchis, *Chem. – Eur. J.*, 2018, **24**, 10468–10474, DOI: **10.1002/chem.201801425**.

51 A. Tuxen, J. Kibsgaard, H. Gøbel, E. Lægsgaard, H. Topsøe, J. V. Lauritsen and F. Besenbacher, *ACS Nano*, 2010, **4**, 4677–4682, DOI: **10.1021/nn1015637**.

52 I. K. Sideri, R. Arenal and N. Tagmatarchis, *ACS Mater. Lett.*, 2020, **2**, 832–837, DOI: **10.1021/acsmaterialslett.0c00108**.

53 I. K. Sideri, R. Canton-Vitoria, H. J. Ojeda-Galvan, M. Quintana and N. Tagmatarchis, *Small*, 2024, **20**, 2311045, DOI: **10.1002/smll.202311045**.

54 R. Canton-Vitoria and R. Kitaura, *Chem. – Eur. J.*, 2024, e202400150, DOI: **10.1002/chem.202400150**.

55 R. Canton-Vitoria, T. Hotta, Y. Tanuma, I. K. Sideri, N. Tagmatarchis, C. Ewels and R. Kitaura, *J. Phys. Chem. C*, 2023, **127**, 10699–10708, DOI: **10.1021/acs.jpcc.2c08009**.

56 R. Canton-Vitoria, S. Nufer, X. Che, Y. Sayed-Ahmad-Baraza, R. Arenal, C. Bittencourt, A. Brunton, A. B. Dalton, C. P. Ewels and N. Tagmatarchis, *Mater. Adv.*, 2020, **1**, 2459–2466, DOI: **10.1039/D0MA00429D**.

57 R. Canton-Vitoria, Y. Sayed-Ahmad-Baraza, M. Pelaez-Fernandez, R. Arenal, C. Bittencourt, C. P. Ewels and

N. Tagmatarchis, *npj 2D Mater. Appl.*, 2017, **1**(1), DOI: **10.1038/s41699-017-0012-8**.

58 T. Umeyama, D. Mizutani, Y. Ikeda, W. R. Osterloh, F. Yamamoto, K. Kato, A. Yamakata, M. Higashi, T. Urakami, H. Sato and H. Imahori, *Chem. Sci.*, 2023, **14**, 11914–11923, DOI: **10.1039/D3SC03604A**.

59 I. K. Sideri, Y. Jang, J. Garcés-Garcés, Á. Sastre-Santos, R. Canton-Vitoria, R. Kitaura, F. Fernández-Lázaro, F. D'Souza and N. Tagmatarchis, *Angew. Chem., Int. Ed.*, 2021, **60**, 9120–9126, DOI: **10.1002/anie.202016249**.

60 R. Canton-Vitoria, T. Scharl, A. Stergiou, A. Cadranel, R. Arenal, D. M. Guldi and N. Tagmatarchis, *Angew. Chem., Int. Ed.*, 2020, **59**, 3976–3981, DOI: **10.1002/anie.201914494**.

61 M. P. Minadakis, R. Canton-Vitoria, C. Stangel, E. Klontzas, R. Arenal, J. Hernandez-Ferrer, A. M. Benito, W. K. Maser and N. Tagmatarchis, *ChemSusChem*, 2023, e202202322, DOI: **10.1002/cssc.202202322**.

62 R. Canton-Vitoria, H. B. Gobeze, V. M. Blas-Ferrando, J. Ortiz, Y. Jang, F. Fernández-Lázaro, Á. Sastre-Santos, Y. Nakanishi, H. Shinohara, F. D'Souza and N. Tagmatarchis, *Angew. Chem., Int. Ed.*, 2019, **58**, 5712, DOI: **10.1002/ange.201900101**.

63 L. Vallan, R. Canton-Vitoria, H. B. Gobeze, Y. Jang, R. Arenal, A. M. Benito, W. K. Maser, F. D'Souza and N. Tagmatarchis, *J. Am. Chem. Soc.*, 2018, **140**, 13488–13496, DOI: **10.1021/jacs.8b09204**.

64 E. Kozma, F. Galeotti, G. Grisci, L. Barba, G. Arrighetti, M. Catellani, G. Scavia and W. Porzio, *Surf. Sci.*, 2018, **675**, 15–25, DOI: **10.1016/j.susc.2018.04.008**.

65 E. Kozma, G. Grisci, W. Mróz, M. Catellani, A. Eckstein-Andicsovà, K. Pagano and F. Galeotti, *Dyes Pigm.*, 2016, **125**, 201–209, DOI: **10.1016/j.dyepig.2015.10.019**.

66 U. Gupta, B. S. Naidu, U. Maitra, A. Singh, S. N. Shirodkar, S. Waghmare and C. N. Rao, *APL Mater.*, 2014, **2**, 092802, DOI: **10.1063/1.4892976**.

67 P. Soubelet, A. E. Bruchhausen, A. Fainstein, K. Nogajewski and C. Faugeras, *Phys. Rev. B*, 2016, **93**, 155407, DOI: **10.1103/physrevb.93.155407**.

68 P. Tonndorf, R. Schmidt, P. Böttger, X. Zhang, J. Börner, A. Liebig, M. Albrecht, C. Kloc, O. Gordan, D. R. Zahn, S. M. de Vasconcellos and R. Bratschitsch, *CLEO*, 2013. DOI: **10.1364/cleoqels.2013.qtu1d.1**.

69 R. Zhang, D. Drysdale, V. Koutsos and R. Cheung, *Adv. Funct. Mater.*, 2017, **27**, 1702455, DOI: **10.1002/adfm.201702455**.

70 R. Srivastava and L. L. Chase, *Solid State Commun.*, 1972, **11**, 349–353, DOI: **10.1016/0038-1098(72)90247-5**.

71 R. Narro-García, *Int. J. Electrochem.*, 2017, 3907–3915, DOI: **10.20964/2017.05.51**.

72 S. Cho, S. Kim, J. H. Kim, J. Zhao, J. Seok, D. H. Keum, J. Baik, D.-H. Choe, K. J. Chang, K. Suenaga, S. W. Kim, Y. H. Lee and H. Yang, *Science*, 2015, **349**, 625–628, DOI: **10.1126/science.aab3175**.

73 X. Ma, P. Guo, C. Yi, Q. Yu, A. Zhang, J. Ji, Y. Tian, F. Jin, Y. Wang, K. Liu, T. Xia, Y. Shi and Q. Zhang, *Phys. Rev. B*, 2016, **94**, 214105, DOI: **10.1103/physrevb.94.214105**.

74 Y. C. Jiang, J. Gao and L. Wang, *Sci. Rep.*, 2016, **6**, 19624, DOI: **10.1038/srep19624**.

75 D. G. Castner, K. Hinds and D. W. Grainger, *Langmuir*, 1996, **12**, 5083–5086, DOI: **10.1039/D1SC02499J**.

76 M. Blanco, M. Lunardon, M. Bortoli, D. Mosconi, L. Girardi, L. Orian, S. Agnoli and G. Granozzi, *J. Mater. Chem. A*, 2020, **8**, 11019–11030, DOI: **10.3390/ma6093826**.

77 F. Wen, F. Zhang, Z. Wang, X. Yu, G. Ji, D. Li, S. Tong, Y. Wang, B. Han and Z. Liu, *Chem. Sci.*, 2021, **12**, 11548–11553, DOI: **10.3390/polym14030359**.

78 D. X. Oh, S. Shin, C. Lim and D. S. Hwang, *Materials*, 2013, **6**, 3826–3839, DOI: **10.1021/la960465w**.

79 Y. Gao, C. Dong, F. Zhang, H. Ma and Y. Li, *Polymers*, 2022, **14**, 359, DOI: **10.1039/d0ta03302b**.

80 S. Golovynskyi, O. I. Datsenko, D. Dong, Y. Lin, I. Irfan, B. Li, D. Lin and J. Qu, *J. Phys. Chem. C*, 2021, **125**, 17806–17819, DOI: **10.1021/acs.jpcc.1c04334**.

81 B. Salhi, F. Vaurette, B. Grandidier, D. Stiévenard, O. Melnyk, Y. Coffinier and R. Boukherroub, *Nanotechnology*, 2009, **20**, 235601, DOI: **10.1088/0957-4484/20/23/235601**.

82 B. Sirota, N. Glavin, S. Krylyuk, A. V. Davydov and A. Voevodin, *Sci. Rep.*, 2018, **8**, 26751, DOI: **10.1038/s41598-018-26751-4**.

83 P. A. Spevack and N. S. McIntyre, *J. Phys. Chem.*, 1992, **96**, 9029–9035, DOI: **10.1021/j100201a062**.

84 R. Canton-Vitoria, T. Hotta, M. Xue, S. Zhang and R. Kitaura, *J. Am. Chem. Soc.*, 2023, 775–784, DOI: **10.1021/jacsau.2c00536**.

85 M. Köppen, *Condens. Matter*, 2019, **4**, 82, DOI: **10.3390/condmat4030082**.

86 R. Canton-Vitoria, K. Sato, Y. Motooka, S. Toyokuni, Z. Liu and R. Kitaura, *Nanoscale*, 2023, **15**, 4570–4580, DOI: **10.1039/d2nr06630k**.

87 R. Coehoorn and C. Haas, *Phys. Rev. B: Condens. Matter Mater. Phys.*, 1987, **35**, 6203–6206, DOI: **10.1103/PhysRevB.35.6203**.

88 W. E. Ford, *J. Photochem.*, 1987, **37**, 189–204, DOI: **10.1016/0047-2670(87)85040-2**.

89 S. Gan, L. Zhong, C. Engelbrekt, J. Zhang, D. Han, J. Ulstrup, Q. Chi and L. Niu, *Nanoscale*, 2014, **6**, 10516–10523, DOI: **10.1039/C4NR02308K**.

90 T. Völzer, A. Schubert, E. von der Oelsnitz, J. Schröer, I. Barke, R. Schwartz, K. Watanabe, T. Taniguchi, S. Speller, T. Korn and S. Lochbrunner, *Nanoscale Adv.*, 2023, **5**, 3348–3356, DOI: **10.1039/D3NA00276D**.

91 S. J. Rowley-Neale, D. A. C. Brownson, G. C. Smith, D. A. G. Sawtell, P. J. Kelly and C. E. Banks, *Nanoscale*, 2015, 7, 18152, DOI: **10.1039/C5NR05164A**.

92 J. Bonde, P. G. Moses, T. F. Jaramillo, J. K. Nørskov and I. Chorkendorff, *Faraday Discuss.*, 2009, **140**, 219–231, DOI: **10.1039/B803857K**.

93 K. Cho, J. Pak, S. Chung and T. Lee, *ACS Nano*, 2019, **13**, 9713–9734, DOI: **10.1021/acsnano.9b02540**.

94 Y. J. Park, A. K. Katiyar, A. T. Hoang and J.-H. Ahn, *Small*, 2019, **15**, 1901772, DOI: **10.1002/smll.201901772**.

95 J. Kang, S. Tongay, J. Zhou, J. Li and J. Wu, *Appl. Phys. Lett.*, 2013, **102**, 012111, DOI: 10.1063/1.4774090.

96 D. Kufer, I. Nikitskiy, T. Lasanta, G. Navickaite, F. H. L. Koppens and G. Konstantatos, *Adv. Mater.*, 2014, **26**, 7226–7232, DOI: 10.1002/adma.201402471.

97 L. Han, M. Yang, P. Wen, W. Gao, N. Huo and J. Li, *Nanoscale Adv.*, 2021, **3**, 2657–2665, DOI: 10.1039/D1NA00073J.

98 S. K. Jain, M. Xian, P. D. Low, P. D. Taylor, S. A. Tawfik, M. J. S. Spencer, S. Kuriakose, A. Arash, C. Xu, S. Sriram, G. Gupta, M. Bhaskaran and S. Walia, *ACS Appl. Electron. Mater.*, 2021, **3**, 2407–2414, DOI: 10.1021/acsaelm.1c00299.

99 X. Xu, Z. Chen, B. Sun, Y. Zhao, L. Tao and J.-B. Xu, *Sci. Bull.*, 2019, **64**, 1700–1706, DOI: 10.1016/j.scib.2019.09.009.

100 H. Liu, F. Gao, Y. Hu, J. Zhang, L. Wang, W. Feng, J. Hou and P. Hu, *2D Mater.*, 2019, **6**, 035025, DOI: 10.1088/2053-1583/ab1c20.

101 Z. Xu, M. He, Q. Wu, C. Wu, X. Li, B. Liu, M. Tang, J. Yao and G. Wei, *Adv. Sci.*, 2023, **10**, 2207743, DOI: 10.1002/advs.202207743.